

# HEAT (MASS) TRANSFER CHARACTERISTICS IN SERPENTINE FLOW PASSAGES WITH A SHARP TURN

Masafumi HIROTA, Hideomi FUJITA, Hiroshi NAKAYAMA  
and Ahmad SYUHADA\*

*Department of Mechanical Engineering*

(Received May 29, 2000)

## Abstract

Heat (mass) transfer characteristics for turbulent flow in rectangular cross-sectioned two-pass channels with a sharp turn have been examined experimentally using the naphthalene sublimation method. It is well known that heat transfer characteristics in such channels are very complex, and they are influenced by many experimental parameters. Among many possible parameters, main attention of this study has been directed to the influence of following four parameters on the heat (mass) transfer characteristics in the channel. (i) Turn clearance, (ii) Reynolds number, (iii) Flow-inlet condition at the channel entrance, (iv) Inclination angle of the partition wall. In this paper, detailed maps of the local Sherwood number distribution are presented, which make clear the complex and steep changes in the local heat/mass transfer rates in and after the sharp turn section and their dependency on these parameters. Then, from a viewpoint of enhancing the mean heat transfer and improving the uniformity of the local heat transfer rates concurrently without an increase of pressure loss, the optimum channel geometry has been determined based on the experimental results.

**Keywords:** forced convection heat transfer, heat exchanger, complex turbulent flow, flow separation and reattachment, secondary flow, naphthalene sublimation technique

---

\*Present address: Department of Mechanical Engineering, Syiah Kuala University, Darussalam, Banda Aceh, Indonesia

## Contents

1. Introduction .....	00
Nomenclature .....	00
2. Influence of Turn Clearance and Reynolds Number .....	00
2.1 Introduction .....	00
2.2 Experimental Apparatus and Procedure .....	00
2.3 Results and Discussion .....	00
2.3.1 Pressure Distribution .....	00
2.3.2 Pressure Loss Coefficient .....	00
2.3.3 Mean Sherwood Number .....	00
2.3.4 Block-Averaged Sherwood Number .....	00
2.3.5 Distribution of Local Sherwood Number .....	00
2.3.6 Influence of Turn Clearance on $Sh$ Distribution .....	00
2.3.7 Influence of Reynolds Number on $Sh$ Distribution .....	00
2.4 Conclusions .....	00
3. Influence of Flow-Inlet Condition .....	00
3.1 Introduction .....	00
3.2 Experimental Apparatus and Procedure .....	00
3.3 Results of Experiments .....	00
3.3.1 Pressure Distribution and Pressure Loss Coefficient .....	00
3.3.2 Mean Sherwood Number .....	00
3.3.3 Block-Averaged Sherwood Number .....	00
3.3.4 Distribution of Local Sherwood Number .....	00
3.4 Discussion .....	00
3.5 Conclusions .....	00
4. Influence of Inclination Angle of Partition (Inner) Wall .....	00
4.1 Introduction .....	00
4.2 Experimental Apparatus and Procedure .....	00
4.3 Results and Discussion .....	00
4.3.1 Mean Sherwood Number and Pressure Loss .....	00
4.3.2 Block-Averaged Sherwood Number .....	00
4.3.3 Local Sherwood Number Distribution for a Medium Turn Clearance .....	00
4.3.4 Influence of Turn Clearance on $Sh$ Distribution .....	00
4.4 Assessment of Heat-Transfer Performance .....	00
4.5 Conclusions .....	00
Acknowledgements .....	00
References .....	00

## 1. Introduction

The thermal efficiency of modern gas-turbine engines strongly depends on the allowable maximum gas temperature at a turbine inlet. The turbine-inlet gas temperature is strongly influenced by the metallurgical limit. Present advanced gas turbines operate at gas entry temperatures much higher than the metal creeping temperatures; therefore, an intensive cooling of blades is required and it is essential to the improvement of the engine performance. Inadequate cooling of the blades can lead to early and disastrous failure of the entire machine; poor heat-exchanging design can cause the hot spots in which melting of the turbine blade may occur, and overcooling can lead to high thermal stresses and again to failure. Therefore, detailed knowledge of heat transfer characteristics

associated with the cooling flow of the turbine blade is necessary to achieve the highest acceptable turbine-blade temperature.

The cooling technology of the gas-turbine blades can be classified into two categories. One is the external cooling that is represented by the film cooling. The other is the internal cooling, in which flow passages of cooling air are shaped inside the turbine blade. In advanced gas-turbine engines, serpentine channels with a rectangular cross-section having sharp 180-degree turns are usually used as an internal flow passage of cooling air [Metzger et al. (1986); Fan et al. (1987); Han et al. (1988); Chyu (1991); Besserman and Tanrikut (1992); Murata et al. (1994); Wang and Chyu (1994); Astarita et al. (1995); Hirota et al. (1997)].

This type of serpentine channel is often used in compact heat exchangers as well. In compact heat exchangers such as the radiators used in automobiles, they usually consist of two reservoir tanks (head tank and bottom tank) and straight flow passages connecting them. If the serpentine channels with a sharp 180-degree turn are used instead of the straight flow passages, only one reservoir tank (head tank) is needed; this contributes much to the downsizing of the heat exchanger.

It is well known that, in such rectangular channel with a 180-degree turn, the secondary flow is induced by the centrifugal force in flowing around the turn section [Johnston (1976)]. Moreover, the separation and reattachment of the flow also occur in and after the sharp turn section [Metzger et al. (1984)]. Thus, the turbulent flow characteristics in the channel become very complex with a three-dimensional structure, and the local heat transfer rates are expected to change steeply over small distances on the heat transfer surface. As mentioned above, the steep variations of the local heat transfer rates increase the thermal stresses and decrease the life of the equipment. Therefore, detailed data on the local heat transfer in the rectangular serpentine channels with a sharp turn are compulsory for the critical design of the gas turbine internal cooling passages, compact heat exchangers, and other thermal equipment used under severe thermal condition. Moreover, those data are also helpful as the database of the heat transfer in complex turbulent flows. In general, however, detailed measurements or numerical predictions of local heat transfer rates for turbulent flow in serpentine channels with a sharp turn are very difficult because of complexities in the channel geometry. Therefore, very few reports have been available to date on the local heat transfer characteristics in those channels.

With these points as background, in this study, detailed characteristics of heat transfer for turbulent flow in the rectangular cross-sectioned serpentine channels with a sharp turn have been examined experimentally using the naphthalene sublimation technique. It has been known that the heat transfer characteristics in such channels are very complex, and they are influenced by many experimental conditions. Among many possible parameters, main attention of this study has been directed to the influence of the following four parameters on the heat (mass) transfer characteristics in the channel; (i) Turn clearance, (ii) Reynolds number, (iii) Flow-inlet condition at the channel entrance, and (iv) Inclination angle of the partition wall. In this paper, the dependency of heat transfer characteristics in the channels on these experimental parameters is described in detail, and the optimum combination of those geometric parameters is examined based on the experimental results.

### Nomenclature

- $C$  = turn clearance, see Fig. 2.3
- $D$  = naphthalene-air molecular diffusion coefficient
- $d_h$  = hydraulic diameter of the channel = 33.3 mm
- $h_m$  = local mass transfer coefficient

$\overline{h}_m$	= mean mass transfer coefficient averaged over whole mass transfer surface
$K$	= pressure loss coefficient, defined by Eq. (2.1)
$P$	= local pressure on the long-side wall
$P_a$	= atmospheric pressure
$Re$	= Reynolds number = $U \cdot d_h / \nu$
$Sh$	= local Sherwood number = $h_m \cdot d_h / D$
$Sh_B$	= block-averaged Sherwood number, defined by Eq. (2.4)
$Sh_m$	= mean Sherwood number averaged over whole test section = $\overline{h}_m \cdot d_h / D$
$Sh_{md}$	= Sherwood number averaged in the downstream half of the test section
$Sh_{mu}$	= Sherwood number averaged in the upstream half of the test section
$U$	= bulk velocity of air = $U_1$ averaged over the channel cross-section
$U_1$	= primary flow velocity
$u_1$	= fluctuating velocity in the streamwise direction
$\alpha$	= inclination angle of the partition wall, see Fig. 4.2
$\nu$	= kinematic viscosity of air
$\rho$	= density of air

## 2. Influence of Turn Clearance and Reynolds Number

### 2.1 Introduction

The flow field in rectangular cross-sectioned channels with sharp 180-degree turns has a complex three-dimensional structure. Therefore, under the forced convection heat transfer, the local heat transfer rates are expected to change steeply in a very complex manner. For a better understanding of the heat transfer characteristics in such channels, it is desirable to measure the local heat transfer rates on all the channel walls at a high spatial resolution and a high data density. Detailed experimental data obtained on all the channel walls provide a better database for the evaluation of the results of computer simulation as well as for the design of high-temperature components. With these points as background, we conducted an experimental study to make clear the detailed local heat (mass) transfer characteristics over all the walls of rectangular channel with a sharp 180-degree turn under the stationary condition [Hirota *et al.* (1999a)].

It is thought that, in such a serpentine channel with a sharp 180-degree turn, the turn clearance (distance between the divider-wall tip and the end wall) and the Reynolds number are most dominant parameters to the flow structure and the local heat transfer. Hence, in this chapter, the results of the pressure measurement and the heat (mass) transfer are presented directing a special attention to the influences of the turn clearance and the Reynolds number on them. Three turn clearances were tested under the Reynolds number range of turbulent flow  $(2.0\text{--}6.0) \times 10^4$ . The naphthalene sublimation method [Goldstein and Cho (1995)] was used to measure the local heat (mass) transfer rates with a sufficiently high spatial resolution and a high density of measuring points. The local pressure distributions on the long-side wall of the channel were measured as well to estimate the characteristics of the flow field.

### 2.2 Experimental Apparatus and Procedure

Figure 2.1 shows a schematic diagram of the experimental apparatus. Since the naphthalene sublimation method was used to measure the local mass transfer rate, the apparatus was operated in a suction mode to exclude a rise in temperature of air caused by a turbofan. Air flows into the test channel through a settling chamber in which the entrance condition of the inlet air flow is set

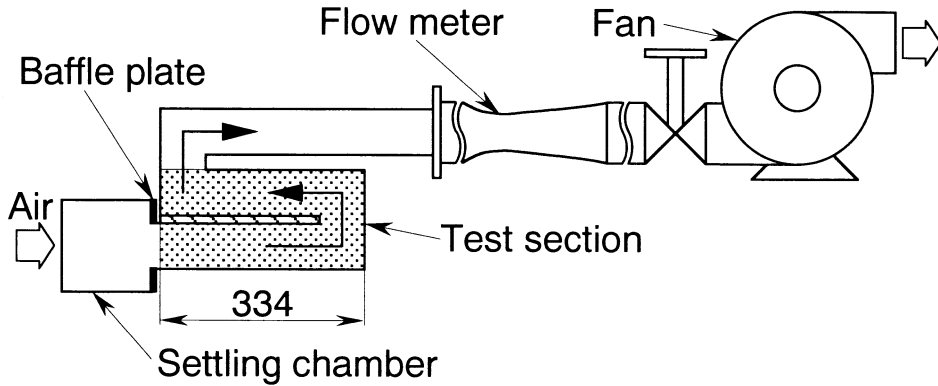


Fig. 2.1 Schematic diagram of the experimental apparatus

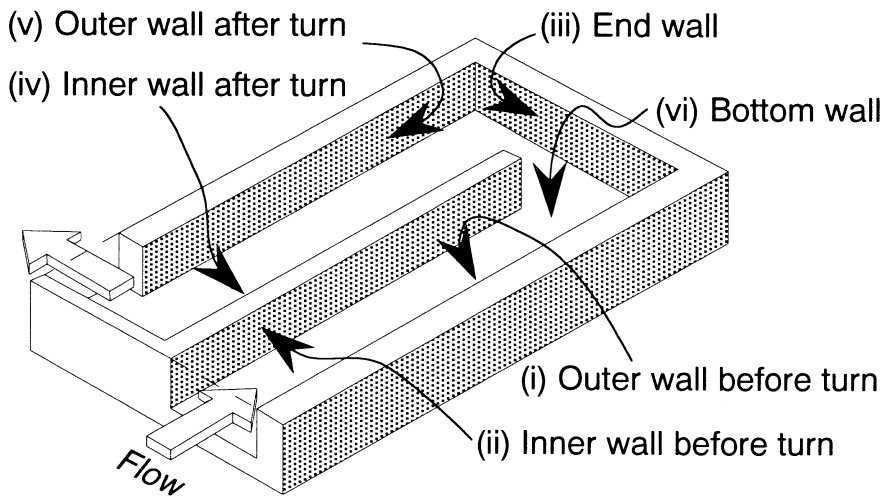


Fig. 2.2 Test section

up. As shown later in detail, a baffle plate is equipped at the entrance of the test channel. The test channel has a rectangular cross-section of  $50 \text{ mm} \times 25 \text{ mm}$  (hydraulic diameter  $d_h = 33.3 \text{ mm}$ ), and has two sharp 180-degree turns. The mass transfer rates and pressure distributions were measured in the darkened region of the figure, which includes the first turn section and is positioned just downstream of the settling chamber. Air contaminated by the naphthalene vapor is then exhausted from the building by a turbofan.

Figure 2.2 shows a schematic illustration of the test section, i.e., the darkened region of Fig. 2.1. In this study, we measured the local mass transfer rates over all the channel walls shown in Fig. 2.2, namely, (i) outer wall before the turn, (ii) inner wall before the turn, (iii) outer wall in the turn (end wall), (iv) inner wall after the turn, (v) outer wall after the turn, and (vi) bottom wall (or top wall). The outer, inner, and end walls are the short-side walls (25 mm width), and the bottom and top walls are the long-side walls (50 mm width). We confirmed that the results obtained on the

top wall agreed well with those on the bottom wall, qualitatively and quantitatively; thus, for the long-side walls, it suffices to show the results on the bottom wall only.

The details of the bottom wall in the test section are shown in Fig. 2.3; the dark region corresponds to the naphthalene surface, and the hatched region is the aluminum frame that supports the naphthalene surface. The partition (inner) wall is 10 mm thick, which divides the naphthalene surface into two straight sections before and after the turn. By changing the length of this partition wall, the turn clearance [distance between the inner-wall tip and the end wall, denoted as “ $C$ ” in Fig. 2.3] can be set at 30 mm, 50 mm or 70 mm. The distance between the channel entrance and the inner-wall tip changes in the range from 264 mm ( $= 7.93 d_h$ ) to 304 mm ( $= 9.13 d_h$ ) depending on the turn clearance. A close-up of the inner-wall tip is also shown in Fig. 2.3. The inner-wall tip has a square configuration and is made of aluminum frame; thus, the regions up to 5 mm from the inner-wall tip on walls (ii) and (iv) are inactive in mass transfer. Figure 2.4 shows the details of the entrance configuration of the channel. A baffle plate was placed at the entrance of the test channel to form a sharp-edged entrance, which ensured that the air flow entering the test section had an abrupt contraction-entrance condition with strong turbulence [Sparrow *et al.* (1982)].

The local mass transfer coefficient  $h_m$  was calculated from the difference in the naphthalene surface profiles before and after each data run, which were measured by a digital linear gage with an accuracy of 1  $\mu\text{m}$ . It was passed over the naphthalene surface by a computer-controlled two-dimensional positioning gear at a 0.2 mm pitch in the streamwise direction and at a 2.5 mm pitch (long-side wall) or 1.25 mm pitch (short-side wall) in the spanwise direction. In each data run, the naphthalene surface was exposed to the air flow for 1–1.5 hours, so that the maximum sublimation depth of the naphthalene surface was less than 0.2 mm. The naphthalene surface was made by a

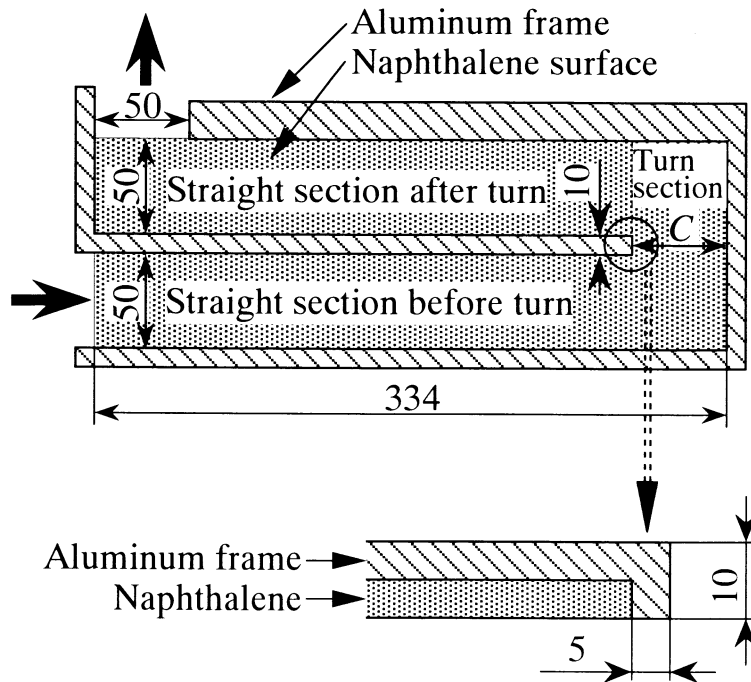


Fig. 2.3 Details of the bottom wall and close-up of the inner-wall tip

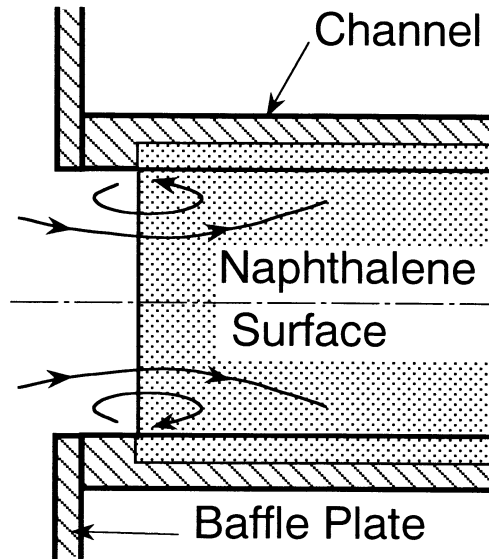


Fig. 2.4 Configuration of the channel entrance

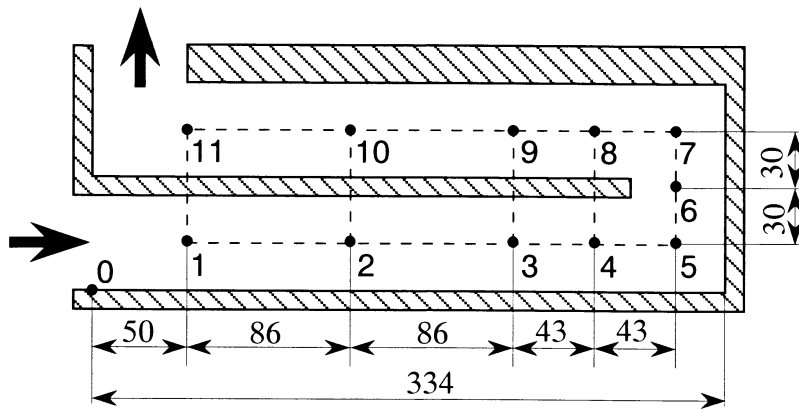


Fig. 2.5 Locations of pressure taps

casting process. In order to produce a hydraulically smooth surface, all the casting processes were carried out in an electric furnace to control the mold temperature accurately; the maximum unevenness of the naphthalene surface was less than  $20\ \mu\text{m}$ , thus the naphthalene surface can be regarded as hydraulically smooth. Details of the naphthalene sublimation method and data processing are described in the reference [Goldstein and Cho (1995)].

The pressure distribution was also measured to estimate the qualitative characteristics of the flow field. The locations of the pressure taps are shown in Fig. 2.5. Twelve pressure taps were distributed in the test section; one pressure tap was on the outer wall near the channel entrance, and eleven taps were on the spanwise centerline of the bottom wall. In addition to the three turn

clearances mentioned above, the pressure distributions were measured for two more turn clearances of  $C = 40$  mm and 60 mm. The mass transfer experiments and pressure measurements were conducted under the Reynolds number  $Re = U \cdot d_h / \nu$  of  $(2.0-6.0) \times 10^4$ , which corresponds to the turbulent flow condition.

## 2.3 Results and Discussion

### 2.3.1 Pressure Distribution

Figure 2.6 shows the distributions of the dimensionless pressure obtained in the channel with a medium turn clearance  $C = 50$  mm for various Reynolds number  $Re$ . The abscissa shows the pressure-tap number defined in Fig. 2.5, and the ordinate shows the dimensionless differential pressure. The flow characteristics in the channel can be estimated qualitatively as follows.

The pressure shows the local minimum at the pressure tap numbered 0 (denoted as Tap 0) that is located near the channel entrance, which then increases once at Tap 1 and decreases monotonously in the flow direction up to Tap 4. This shows that the flow is separated at the edge of the baffle plate, and that the separated flow reattaches on the channel walls causing the pressure recovery at Tap 1, with the resulting pressure loss caused by the wall friction after Tap 1. At Tap 5, located in the upstream half of the turn section, the pressure slightly increases; this pressure rise is caused by the impingement of the flow, which enters the turn section through the straight section, against the end wall (wall (iii) in Fig. 2.2).

After the pressure reaches its local minimum at Tap 6, it increases once at Tap 7 and then decreases very steeply to attain the minimum at Tap 8. This complex change in pressure distribution suggests that the flow is separated at the tip of the partition (inner) wall and that a separation bubble is formed in the straight section after the turn. The pressure rise observed at Tap 7 is attrib-

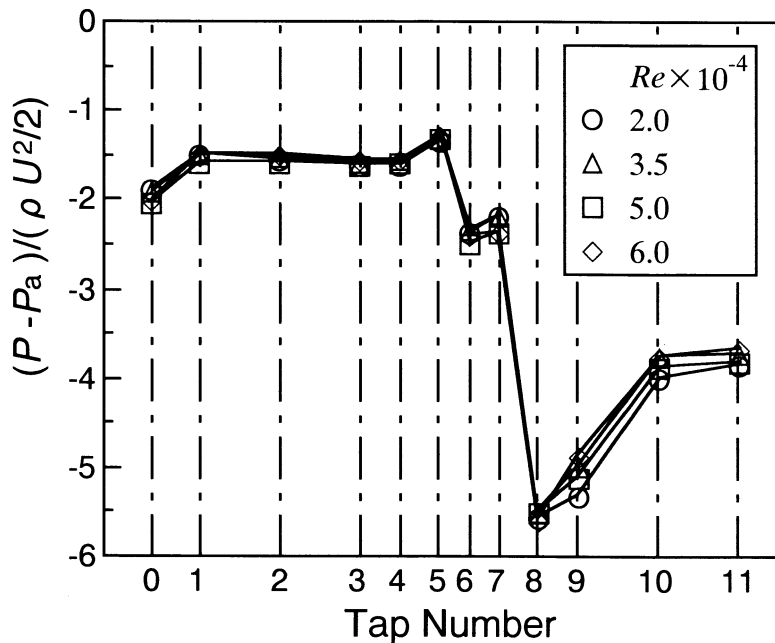


Fig. 2.6 Pressure distributions for different  $Re$  ( $C = 50$  mm)

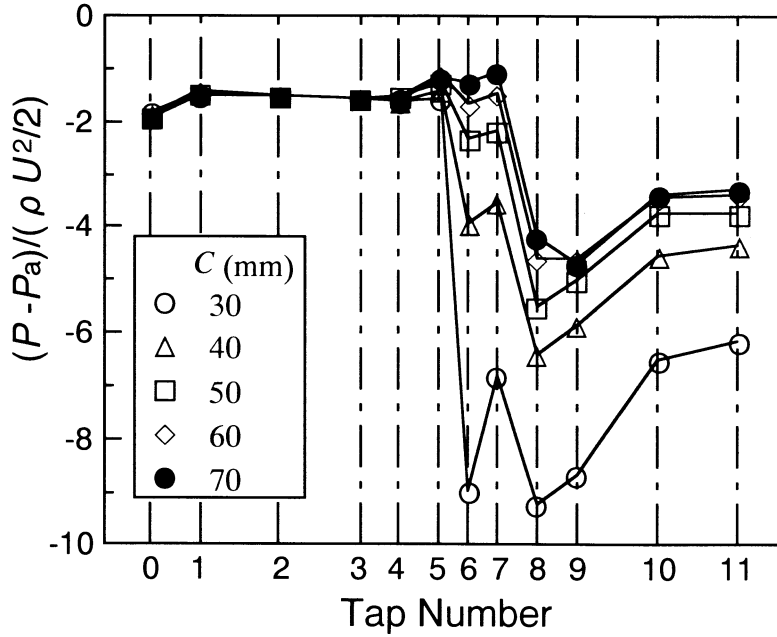


Fig. 2.7 Pressure distributions for different  $C$  ( $Re = 3.5 \times 10^4$ )

uted to the impingement of the flow passing through the turn clearance against the outer wall (wall (v) in Fig. 2.2); this mechanism of pressure rise is similar to that encountered at Tap 5. The pressure recovers after the separation bubble, and it approaches an asymptotic value at Tap 11.

Figure 2.7 shows a comparison of the dimensionless pressure distributions obtained for different turn clearances at a constant  $Re$  of  $3.5 \times 10^4$ . The pressure at Tap 6 diminishes as the turn clearance is decreased, because the decrease in the turn clearance causes an acceleration of the flow passing through it. The difference in the pressures at Tap 6 and Tap 8 becomes smaller with the decrease in the turn clearance, whereas the pressure difference between Tap 7 and Tap 8 is almost constant irrespective of the turn clearance except for the case of  $C = 30$  mm. It can be estimated that the flow structure after the turn for  $C = 30$  mm has some unique characteristics which are different from those for larger turn clearances.

### 2.3.2 Pressure Loss Coefficient

Based on the pressure distributions shown above, the pressure loss coefficient  $K$ , which is defined by the following equation, was calculated.

$$K = \frac{2 \cdot (P_0 - P_{11})}{\rho_a U^2} \quad (2.1)$$

$P_0$  denotes the static pressure at the channel entrance, and  $P_{11}$  is that measured at Tap 11 that is located near the exit of the test section. Since  $P_0$  could not be measured directly in the present channel due to the flow separation at the channel entrance, it was obtained by applying Bernoulli's equation to the flow far from the channel entrance and that at the channel entrance. Air far from

the channel entrance is stationary and in the atmospheric pressure  $P_a$ . Assuming that the flow velocity at the channel entrance is equal to the bulk air velocity  $U$ ,  $P_0$  is thus given by the following equation.

$$P_0 = P_a - \frac{\rho_a U^2}{2} \quad (2.2)$$

Consequently,  $K$  is expressed as follows.

$$K = \frac{2 \cdot (P_a - P_{11})}{\rho_a U^2} - 1 \quad (2.3)$$

Figure 2.8 shows the variations of  $K$  against  $Re$ .  $K$  is nearly constant against  $Re$ , and  $C$  is decisive for  $K$ -values. The values of  $K$  generally increase as the turn clearance is decreased, and those for  $C = 30$  mm are significantly larger than those for wider turn clearances. The solid symbols in the figure show the results obtained by Metzger *et al.* (1984) in the channel which is equivalent to that of  $C = 50$  mm in the present experiment. The present results of  $K$  for  $C = 50$  mm agree well with their results.

### 2.3.3 Mean Sherwood Number

The Sherwood number averaged over the whole naphthalene surface in the test section, i. e., mean Sherwood number and denoted as  $Sh_m$ , was calculated from the total amount of naphthalene sublimated during a data run. Figure 2.9 shows the variations of  $Sh_m$  versus Reynolds number obtained for the medium turn clearance in the present experimental condition  $C = 50$  mm. In addition

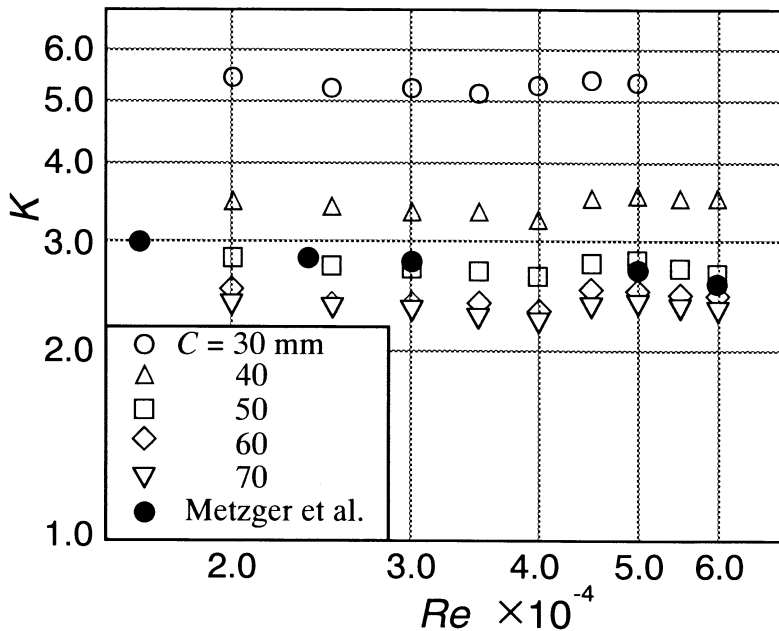
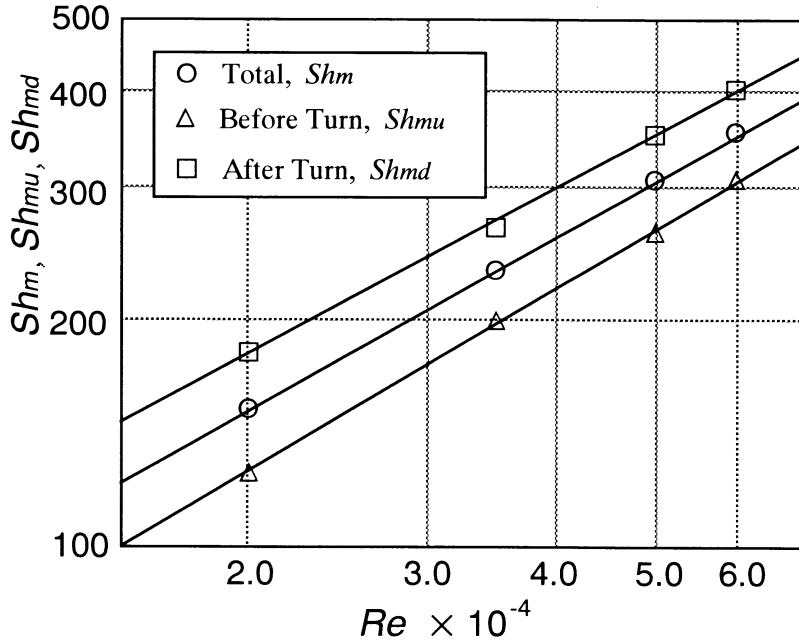


Fig. 2.8 Coefficients of pressure loss

Fig. 2.9 Mean Sherwood numbers ( $C = 50$  mm)

to  $Sh_m$ , the Sherwood numbers averaged in the upstream and the downstream halves of the test section, denoted as  $Sh_{mu}$  and  $Sh_{md}$ , respectively, are also shown in the figure.  $Sh_m$ ,  $Sh_{mu}$ , and  $Sh_{md}$  increase in proportion to  $Re^n$  ( $n = 0.8-1.0$ ). The values of  $Sh_{md}$  are 1.3–1.4 times as large as those of  $Sh_{mu}$ ; this means that the mass-transfer-enhancement effect of the sharp turn is greater than that of the sharp-edged entrance.

Qualitatively similar results have been obtained in other test channels with different turn clearances. From a quantitative viewpoint, the values of  $Sh_m$ ,  $Sh_{mu}$ , and  $Sh_{md}$  in the channel with the widest turn clearance of  $C = 70$  mm were almost the same as those for  $C = 50$  mm, while  $Sh_m$  and  $Sh_{md}$  for the narrowest turn clearance of  $C = 30$  mm were 1.2 times and 1.3 times as large as those for  $C = 50$  mm, respectively. It is thought that the flow acceleration in passing through the narrow turn clearance enhanced the mass transfer after the turn.

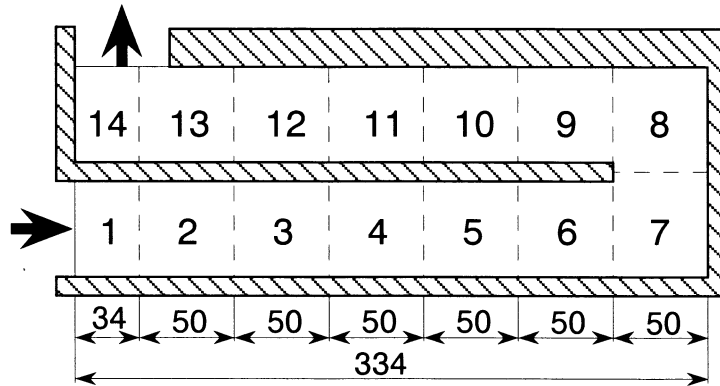
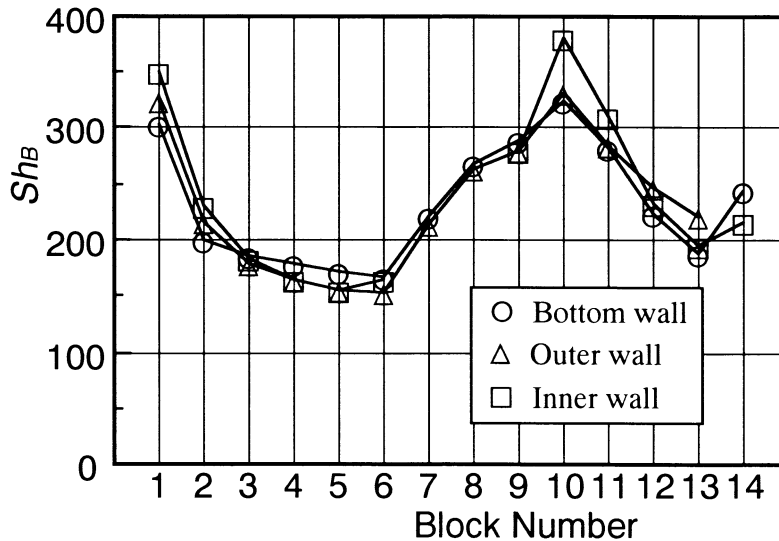
### 2.3.4 Block-Averaged Sherwood Number

In order to obtain an overall view of the local mass transfer characteristics in the channel, we divided the test section into 14 blocks as shown in Fig. 2.10 and calculated the integral-average of the local Sherwood number in each block on each channel wall. This block-averaged Sherwood number,  $Sh_B$ , is thus defined by the following equation,

$$Sh_B = \frac{1}{\Delta S} \iint_{\Delta S} Sh \, dS \quad (2.4)$$

where  $\Delta S$  denotes the surface area of each block.

Figure 2.11 shows the typical streamwise variations in  $Sh_B$  obtained on each channel wall for

Fig. 2.10 Definition of blocks ( $C = 50$  mm)Fig. 2.11 Block-averaged Sherwood numbers on each channel wall ( $C = 50$  mm)

$C = 50$  mm and  $Re = 3.5 \times 10^4$ . The abscissa shows the block-numbers defined in Fig. 2.10. As a general trend, the characteristics of  $Sh_B$  distributions, such as the locations and values of maximum  $Sh_B$ , on the bottom wall agree well with those on the outer and inner walls. Thus it follows that, for the purpose of grasping the outline of the  $Sh_B$  distributions, it is enough to measure the mass transfer rates on either the long-side wall or the short-side walls.

$Sh_B$  shows the maximum in Block 1 located at the entrance of the test section, then decreases in the flow direction because of the development of the concentration boundary layer, and reaches minimum in Block 6.  $Sh_B$  then increases in the turn section, i.e., Blocks 7 and 8, and attains its local maximum in Block 10 which is located one block downstream of the turn exit. This location of the local maximum  $Sh_B$  agrees well with that reported by Chyu (1991). It should be noted that,

although the values of  $Sh_b$  in Block 10 are almost the same as those in Block 1,  $Sh_b$ -values in Block 11 are much larger than those in Block 2. This suggests that the mass-transfer-enhancement effect of the sharp turn is maintained over a longer distance after the turn than the effect of the abrupt-contracted flow inlet is maintained after the channel entrance. This difference in the effective lengths is reflected on the difference between  $Sh_{mu}$  and  $Sh_{md}$  observed in Fig. 2.9. In Block 10,  $Sh_b$  on the inner wall is larger than that on the other walls; as described in detail later, this high mass transfer rate is caused by the reattachment of the flow, which is separated at the inner-wall tip, on the inner wall.  $Sh_b$  increases again in Block 14 due to the influence of the second sharp turn located at the end of the test section.

Figures 2.12(a), 2.12(b), and 2.12(c) show the  $Sh_b$  distributions on the bottom wall, outer wall, and inner wall of the channel, respectively, obtained for different turn clearances. In Fig. 2.12(b), Blocks 7 and 8 are located on the outer walls (i) and (v) (see Fig. 2.2), respectively, and Blocks 7e and 8e are on the end wall (iii). As a whole, the values of  $Sh_b$  for  $C = 50$  mm are nearly equal to those for  $C = 70$  mm on all the walls. On the bottom and outer walls,  $Sh_b$ -values for  $C = 30$  mm are notably larger than those for the other channels after Block 7 (Fig. 2.12(a)) and Block 7e (Fig. 2.12(b)). However, on the inner wall shown in Fig. 2.12(c), the influence of  $C$  on  $Sh_b$ -values is less pronounced than that observed in Figs. 2.12(a) and 2.12(b). On the bottom and inner walls, similarly to Fig. 2.11, the local maximum of  $Sh_b$  appears in Block 10 irrespective of the turn clearance. However, on the outer wall for  $C = 30$  mm, the local maximum of  $Sh_b$  appears in Block 8 as well as Block 10.

### 2.3.5 Distribution of Local Sherwood Number

Figure 2.13 shows the typical distributions of the local Sherwood number  $Sh$  which were obtained under a standard experimental condition in this study, i. e., medium turn clearance  $C = 50$  mm and medium Reynolds number  $Re = 3.5 \times 10^4$ . In this section, the general characteristics of the local heat (mass) transfer obtained in this standard test case are described in detail based on Fig. 2.13. The figure consists of six maps, (i) to (vi), showing the  $Sh$  distributions obtained on each channel wall illustrated in Fig. 2.2. The variations in  $Sh$ -values are shown as contrasting light and dark areas of various shading; the maps become whiter as the values of  $Sh$  are increased, and the regions of  $Sh > 400$  are shown in white. The arrows indicate the flow directions at the entrance or exit of each section. In Fig. 2.14, the schematic illustration of the time-mean surface flow on each wall is shown, which was estimated from the pressure distributions (Fig. 2.6) and the local mass transfer characteristics.

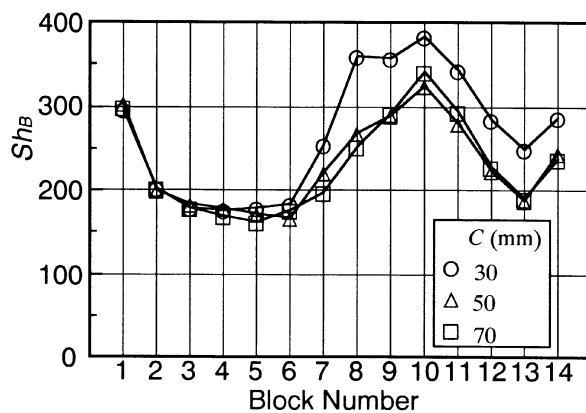
In this section, the characteristics of  $Sh$  distributions are described in detail by dividing the test channel into the following three sections; (1) straight section before the turn (Blocks 1 to 6 in Fig. 2.10), (2) turn section (Blocks 7 and 8), and (3) straight section after the turn (Blocks 9 to 14).

#### (1) Straight section before the turn

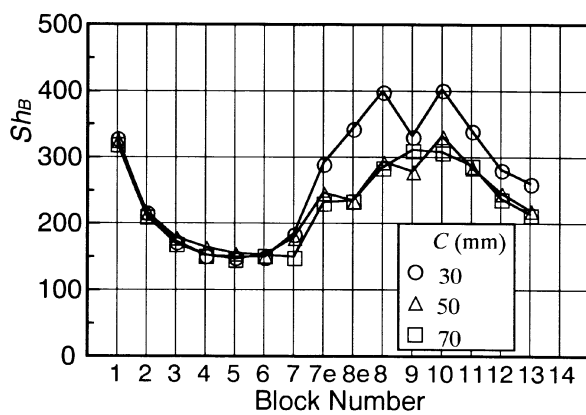
At the entrance of the channel,  $Sh$  shows the local maximum on both the short-side and long-side walls; these large mass transfer rates are caused by the strong turbulence produced at the sharp-edged entrance and by the leading-edge effect of the boundary layer.  $Sh$  then decreases gradually in the flow direction due to the development of the concentration boundary layer on each channel wall.  $Sh$  distributions on the bottom wall agree well with those on the outer and inner walls, qualitatively and quantitatively. Therefore, it follows that the local mass transfer in this section shows two-dimensional characteristics in spite of the flow field that is estimated to have a three-dimensional structure.

#### (2) Turn section

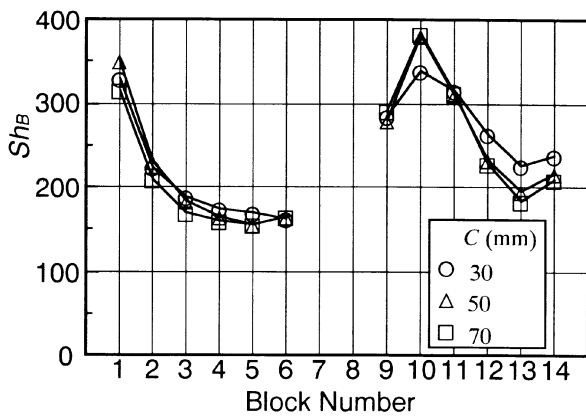
At first,  $Sh$  distributions in the upstream half of the turn section, i.e., Block 7 in Fig. 2.10, are examined in detail. On the bottom wall shown in Fig. 2.13 (vi),  $Sh$  increases gradually in the flow direction, then rises very steeply to attain its local maximum near the junction with the end wall.



(a) Bottom wall



(b) Outer wall



(c) Inner wall

Fig. 2.12 Block-averaged Sherwood numbers for different  $C$  ( $Re = 3.5 \times 10^4$ )

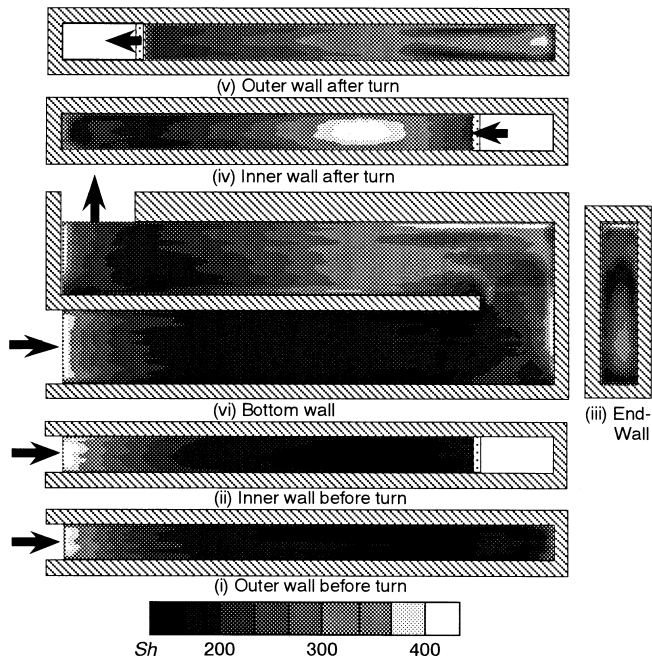


Fig. 2.13 Local Sherwood number distribution ( $C = 50$  mm,  $Re = 3.5 \times 10^4$ )

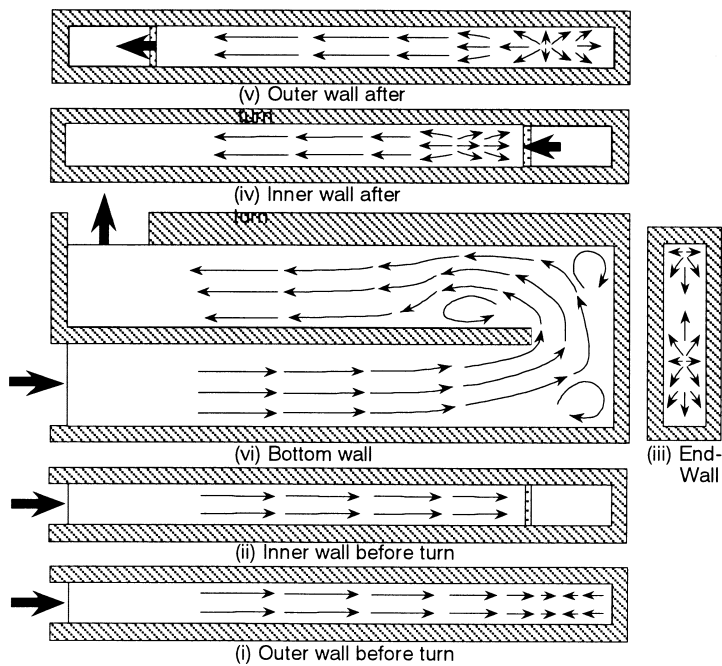


Fig. 2.14 Schematic illustration of surface flow ( $C = 50$  mm)

The relatively gradual increase in  $Sh$  mentioned in the former is caused by the secondary flow, which transports fresh air from the core region with low naphthalene-vapor concentration to the vicinity of the bottom wall.

On the end wall shown in Fig. 2.13 (iii),  $Sh$  attains the local maximum near the center of Block 7e; this high  $Sh$  region is brought about by the impingement of the flow that enters the turn section through the straight section before the turn. The impinging flow is then forced to change its direction by the end wall, and impinges again on the bottom wall (see the end-wall in Fig. 2.14). This “secondary” flow-impingement causes the local maximum of  $Sh$  on the bottom wall described above. On the other hand, in the corner of the bottom wall and the end wall, there appears a region of low  $Sh$ -values. This suggests that, near the corner in the upstream half of the turn section, the flow separation occurs due to the abrupt change in the flow direction at the sharp turn, resulting in the formation of a recirculation zone of low mass transfer rates [Metzger *et al.* (1984); Wagner *et al.* (1991); Liou, *et al.* (1999)].

In the downstream half of the turn section, i.e., Block 8, the values of  $Sh$  on the bottom wall are larger than those in Block 7. This enhancement of local mass transfer is caused by an increase in the primary flow velocity, which occurs due to the flow separation at the inner-wall tip and a resultant decrease in the substantial cross-sectional area of the flow passage. This accelerated flow passing through the turn clearance then impinges on the outer wall after the turn, wall (v) in Fig. 2.2, and thus  $Sh$  attains its local maximum near the upstream edge of this wall. Similarly to the case of Block 7, the direction of this impinging flow is changed by the outer wall, then the flow blows down on the bottom wall (see wall (v) in Fig. 2.14). Thus,  $Sh$  in Block 8 on the bottom wall shows quite large values along the junctions with the outer wall. On the end wall,  $Sh$  decreases once in the flow direction after its local maximum in Block 7e, but it increases again to its local maximum near the downstream edge of the wall. This suggests that the above-mentioned flow impinging on the outer wall is partially reversed toward the end wall and enhances the mass transfer in Block 8e.

### (3) *Straight section after the turn*

Since the flow exiting the turn section is separated at the tip of the partition (inner) wall, a separation bubble is formed along the inner wall after the turn [Metzger *et al.* (1984)]. The mass transfer is deteriorated in this separation bubble due to the recirculation of the flow, and thus  $Sh$  on the inner wall (Fig. 2.13 (iv)) and on the bottom wall reaches its local minimums near the tip of the inner wall. On the other hand, in Block 9 on the outer wall (Fig. 2.13 (v)), the region of relatively high  $Sh$ -values still remains near the spanwise centerline of the wall after the local maximum in Block 8.

In Block 10,  $Sh$  attains its local maximum on all the channel walls, corresponding to the local maximums of  $Sh_B$  in Fig. 2.11. It is thought that such large mass transfer rates in Block 10 are caused by the reattachment of the flow which is separated at the inner-wall tip [Metzger *et al.* (1984); Wang *et al.* (1994)]. On the bottom wall, the region of high  $Sh$ -values occupies most of Block 10, and no spanwise deviations are observed clearly in the  $Sh$  distribution. On the other hand, on the short-side walls,  $Sh$ -values on the inner wall are larger than those on the outer wall if compared at the same streamwise location in Block 10. It is thought that the flow separated at the inner-wall tip is unsteady, and that the location of the flow reattachment can change over time. From the  $Sh$  distributions on the short-side walls shown here, it follows that under the present experimental condition the separated flow reattaches on the inner wall, in Block 10, in the sense of time-mean location averaged during the period of data run.

After Block 11,  $Sh$  decreases gradually as the flow proceeds downstream. A detailed comparison of  $Sh$  distributions obtained at an equal streamwise location reveals that the values of  $Sh$  in the outer-wall side are larger than those in the inner-wall side. This spanwise non-uniformity of  $Sh$  distribution suggests that the flow field after the turn section has a deflection in the primary flow

with higher velocity toward the outer wall.

### 2.3.6 Influence of Turn Clearance on $Sh$ Distribution

In this section, the influence of the turn clearance on the local mass transfer characteristics is examined in detail by showing the results obtained in the test channels of  $C = 30$  mm and  $C = 70$  mm. At first, Fig. 2.15 shows the  $Sh$  distributions obtained in the channel with a narrower turn clearance of  $C = 30$  mm for  $Re = 3.5 \times 10^4$ . In the upstream half of the turn section (Block 7), the region of high  $Sh$ -values occupies a rather large area on the bottom wall near the junction with the end wall, and the recirculation zone of low  $Sh$ , such as observed in the corner of Fig. 2.13 (vi), almost disappears. These results show that the influence of decreasing  $C$  on the  $Sh$  distribution appears in the regions not only downstream but also upstream of the turn clearance.

In the downstream half of the turn section, the mass transfer is much enhanced on all the walls. This is because the flow impinging on the outer wall is accelerated by reducing the turn clearance and, as a result, the flows blowing down on the bottom wall and reversed to the end wall after impinging on the outer wall have higher velocities. Near the streamwise midpoint of the end wall, however,  $Sh$  reaches its local minimum as in the case of  $C = 50$  mm, and its value is almost the same as that shown in Fig. 2.13 (iii).

In the straight section after the turn, the values of  $Sh$  are much larger than those in Fig. 2.13 to the exit of the test section; this suggests that the effect of reducing the turn clearance on  $Sh$  is maintained down to the region located far from the turn section. As in the case of  $C = 50$  mm, the low mass transfer region corresponding to the separation bubble is formed along the inner wall near its tip, and  $Sh$  attains the local maximum in Block 10. The local mass transfer characteristics in and after Block 10 are, however, remarkably different from those for  $C = 50$  mm. In Figs. 2.13 (iv) and 13 (v),  $Sh$ -values in Block 10 on the inner wall were larger than those on the outer wall, and thus it was estimated that the flow which is separated at the inner-wall tip reattaches on the inner wall. In contrast, in Block 10 of the present channel with  $C = 30$  mm, the local maximum of  $Sh$  on the outer wall is larger than that on the inner wall. This means that, as opposite to the case of  $C = 50$  mm, the flow separated at the inner-wall tip reattaches on the outer wall in the present channel. After the flow reattachment, the deflection of the high  $Sh$  region to the outer-wall side is also observed to be similar to the case of  $C = 50$  mm, but the spanwise non-uniformity of  $Sh$  distribution observed in Fig. 2.15 (vi) is more pronounced than that in Fig. 2.13 (vi).

Next, the distributions of  $Sh$  obtained for the largest turn clearance of 70 mm are shown in Fig. 2.16. In the upstream (first) corner of the turn section, the region of low  $Sh$ -values corresponding to the recirculation zone occupies a larger area on the bottom and end walls than that for the smaller turn clearances. On the end wall,  $Sh$  shows the local maximum in Block 7e as similar to the other channels. However, the second local maximum that was observed in Block 8e of Figs. 2.13 (iii) and 2.15 (iii) does not appear so clearly in Fig. 2.16 (iii); it can be observed in a very narrow region immediately close to the downstream (second) corner. Moreover, in Block 8 on the outer wall,  $Sh$  is not as high as that in the other channels.

Downstream of the separation bubble that exists along the inner wall after the turn,  $Sh$  attains its local maximum in Block 10 as similar to Figs. 2.13 and 15. In Block 10, the values of  $Sh$  on the inner wall are much larger than those on the outer wall, suggesting that the flow which separated at the inner-wall tip reattaches on the inner wall as in the case of  $C = 50$  mm. Moreover, a detailed comparison of Figs. 2.13, 2.15, and 2.16 reveals that the local maximum of  $Sh$  on the short-side wall after the separation bubble appears around the center of Block 10 irrespective of the difference in the turn clearance. This means that the streamwise distance from the flow separation, i.e., inner-wall tip, to the flow reattachment becomes shorter as the turn clearance is increased.

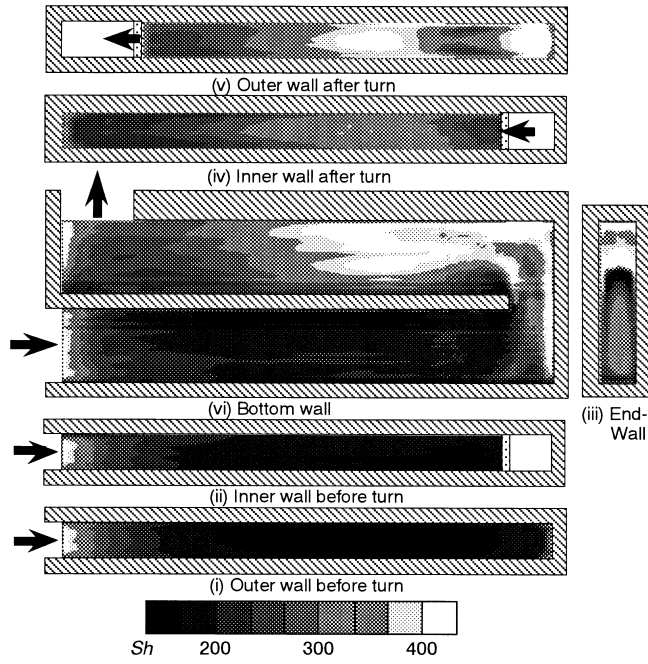


Fig. 2.15 Local Sherwood number distribution ( $C = 30 \text{ mm}$ ,  $Re = 3.5 \times 10^4$ )

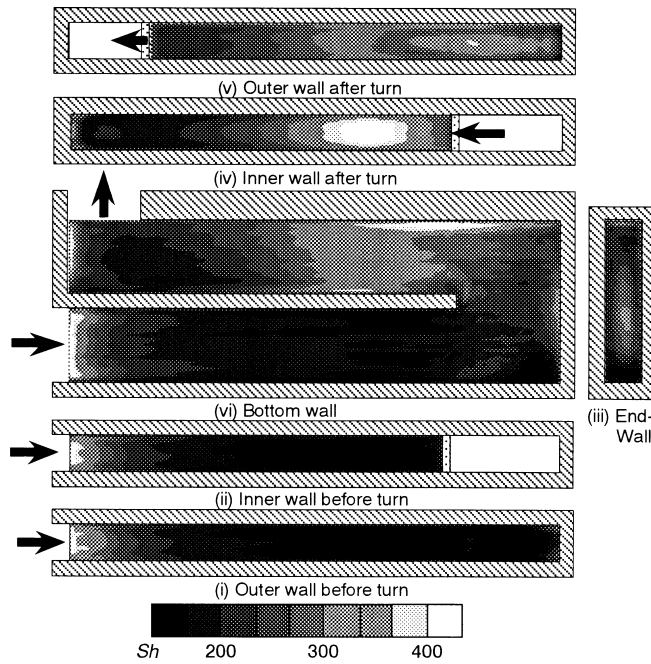


Fig. 2.16 Local Sherwood number distribution ( $C = 70 \text{ mm}$ ,  $Re = 3.5 \times 10^4$ )

### 2.3.7 Influence of Reynolds Number on $Sh$ Distribution

Figure 2.17 shows the  $Sh$  distributions obtained in the same channel as Fig. 2.13 ( $C = 50$  mm) under a smaller Reynolds number of  $2.0 \times 10^4$ , and Fig. 2.18 shows those for a larger  $Re$  of  $5.0 \times 10^4$ . In the straight section before the turn and in the turn section, the  $Sh$  distributions on all the channel walls of Figs. 2.13, 2.17, and 2.18 agree qualitatively well with one another. After the turn section, however, the influence of the Reynolds number on the  $Sh$ -distribution can be described as follows.

Under a lower  $Re$ ,  $Sh$  on the inner wall shown in Fig. 2.17 (iv) attains its local maximum in Block 10 after the separation bubble in Block 9; whereas on the outer wall of Fig. 2.17 (v), the values of  $Sh$  in Block 10 are not as large as those on the inner wall. Such characteristics of  $Sh$  distribution are similar to those observed under  $Re = 3.5 \times 10^4$  described in Section 2.3.5. On the other hand, in Block 10 of Fig. 2.18 for a larger  $Re$ , the difference between the  $Sh$ -values on the inner and outer walls is not so large as that observed in Block 10 for smaller  $Re$  (Figs. 2.13 and 2.17).

A similar trend as described here was also observed in the channel of larger turn clearance  $C = 70$  mm. In the case of narrow turn clearance of  $C = 30$  mm, however, the values of  $Sh$  in Block 10 on the outer wall were much larger than those on the inner wall under any  $Re$  tested here, and the qualitative characteristics of  $Sh$  distribution were independent of the Reynolds number. From these results,  $Re$ -dependency of the flow field in the present channels can be estimated as follows. In the channel with a relatively large turn clearance, the flow which separated at the inner-wall tip mostly reattaches on the inner wall under a low  $Re$  condition. As  $Re$  is increased, however, the unsteadiness of the flow after the turn is intensified, and this separated flow tends to occasionally reattach on the outer wall as well as on the inner wall. On the other hand, in the channel with a

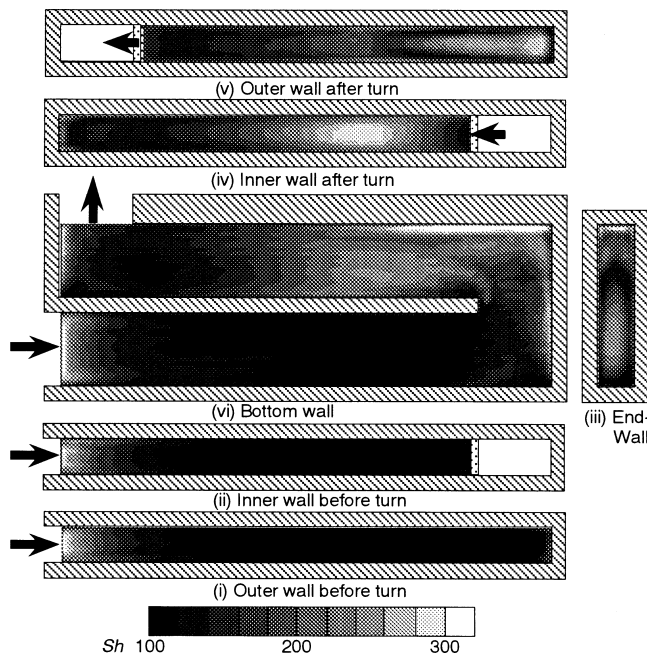


Fig. 2.17 Local Sherwood number distribution ( $C = 50$  mm,  $Re = 2.0 \times 10^4$ )

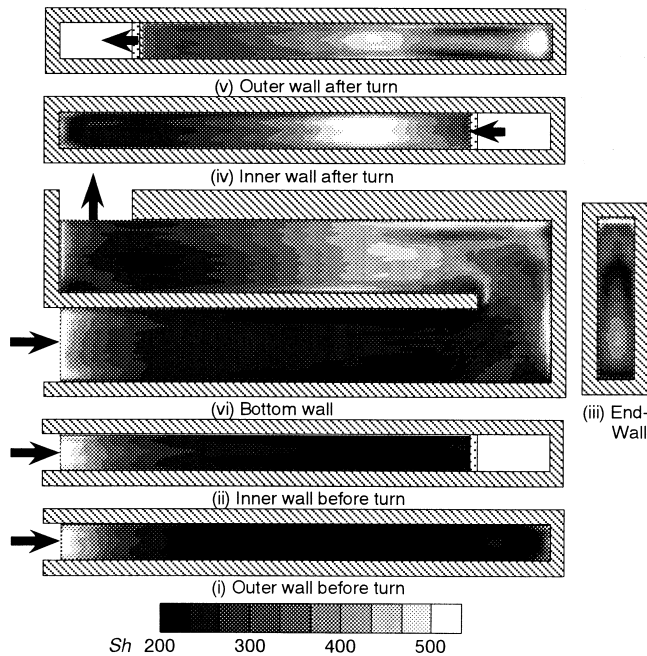


Fig. 2.18 Local Sherwood number distribution ( $C = 50$  mm,  $Re = 5.0 \times 10^4$ )

small turn clearance, the unsteadiness of the flow reattachment is weaker than in the case of a larger turn clearance, and the flow field after the turn is somewhat insensitive to the Reynolds number.

## 2.4 Conclusions

In this chapter, general characteristics have been described on the forced convection heat (mass) transfer in a rectangular channel with a sharp 180-degree turn under a standard experimental condition with  $C = 50$  mm and  $Re = 3.5 \times 10^4$ . Then, the influences of the turn clearance and Reynolds number on the local heat (mass) transfer characteristics have been examined in detail. The main results can be summarized as follows.

(1) In all the channels tested in this chapter, the mean Sherwood number  $Sh_m$  increases in proportion to  $Re^n$  ( $n = 0.8-1.0$ ), and the Sherwood number averaged in the downstream half of the test section is 1.3–1.4 times as large as that of the upstream half. The values of  $Sh_m$  for  $C = 70$  mm are almost the same as those for  $C = 50$  mm, whereas  $Sh_m$  for  $C = 30$  mm is 1.3 times as large as that for  $C = 50$  mm.

(2) The global distributions of the block-averaged Sherwood number  $Sh_B$  on the long-side wall are quite similar to those on the short-side walls, and the maximum  $Sh_B$  is observed in Block 10 a few  $d_h$  downstream of the inner-wall tip irrespective of the turn clearance. On the outer wall and bottom wall,  $Sh_B$ -values for  $C = 30$  mm are larger than those for other channels in and after the turn section. On the partition (inner) wall, however, the influence of  $C$  on  $Sh_B$  does not appear as clearly as on the other walls.

(3) In the turn section, the local Sherwood number  $Sh$  becomes much larger than that in the straight section before the turn, but the recirculation zone of low  $Sh$ -values appears in the upstream

(first) corner of the turn. On the end wall, there appear two local maximums of  $Sh$ ; the first one is observed in the upstream half of the wall, and the second one appears near the downstream edge of the wall. In the channel of  $C = 70$  mm, however, the latter appears in a very narrow region near the downstream (second) corner and is not so clear as that in the other channels.  $Sh$  also attains its local maximum on the outer wall in the downstream half of the turn section due to the flow that impinges against this wall after passing through the turn clearance.

(4) In the straight section after the turn, the flow which is separated at the inner-wall tip forms a separation bubble along the inner wall, and low  $Sh$  regions corresponding to it appear on the bottom and inner walls. In the channels of  $C = 50$  mm and 70 mm under a relatively low  $Re$ , this separated flow reattaches on the inner wall (in Block 10) where  $Sh$  attains its local maximum. As  $Re$  is increased, however, the local maximums of  $Sh$  tend to appear not only on the inner wall but also the outer wall. In the channel of  $C = 30$  mm, the separated flow reattaches on the outer wall irrespective of  $Re$ . In all the channels tested here,  $Sh$  in the outer-wall side shows larger values than that in the inner-wall side in the region after the flow reattachment.

### 3. Influence of Flow-Inlet Condition

#### 3.1 Introduction

In Chapter 2, the distributions of local Sherwood numbers obtained on all the channel walls of the rectangular cross-sectioned serpentine channels with a sharp 180-degree turn were presented, directing special attention to the influences of the turn clearance and Reynolds number. In the experiment described there, the baffle plate was settled at the channel entrance and the air flow entering the test channel was forcibly separated there.

In applying those serpentine channels to practical thermal equipment, such as the internal cooling passages of gas-turbine blade and the flow passages of compact heat exchangers, fluid may be supplied to the channels under various inlet conditions at the entrance; the inlet flow can have variety of velocity distributions, boundary-layer thicknesses, turbulence intensities, etc. [Burggraf (1970)]. In general, the serpentine channel used in such thermal equipment has a rather short straight section before the turn. Thus, the flow in it is in the developing condition, and the flow characteristics not only before the turn but also in and after the turn can be significantly influenced by the flow-inlet condition. As a result, it is possible that whole characteristics of the local heat transfer in the serpentine channel are also influenced by the flow-inlet condition through the change of the flow structure. Therefore, it is of fundamental interest and practical importance to elucidate the influence of the flow-inlet condition on heat transfer characteristics in the serpentine channel with a sharp turn.

Hence, in this study, we made an attempt to make clear experimentally the influence of the flow-inlet condition on the local heat transfer characteristics in rectangular cross-sectioned serpentine channels with a sharp 180-degree turn [Hirota et al. (1999b)]. Two contrastive flow-inlet conditions, contracted-flow inlet (inlet condition adopted in Chapter 2) and uniform-flow inlet, were tested in this study; these conditions are considered to cover the usual extremes encountered in practical equipment [Kays and Crawford (1980)]. Under these flow-inlet conditions, detailed distributions of local heat (mass) transfer rates in the serpentine channels were measured by the naphthalene sublimation method.

#### 3.2 Experimental Apparatus and Procedure

The flow loop and test channels are essentially the same as those used in the experiments

described in Chapter 2, except for the flow-inlet condition at the channel entrance. Two contrastive flow-inlet conditions were applied in this study. Details of the entrance configurations are shown in Fig. 3.1. One is the “contracted-flow inlet” [Fig. 3.1(a)] which is the same condition as adopted in the experiment in Chapter 2; a baffle plate is placed at the entrance of the test channel to form a sharp-edged entrance. The air flow entering the test section is separated at the edge of this baffle plate and thus has an abrupt contraction-entrance condition with strong turbulence [Sparrow *et al.* (1982)]. The other is the “uniform-flow inlet” condition [Fig. 3.1(b)]; air is supplied to the channel through a nozzle which is designed carefully to make the boundary-layer thickness at its exit as thin as possible. We confirmed that, with this nozzle, the inlet flow had a highly uniform velocity distribution over the channel cross-section at the entrance, and that the turbulence level was as low as 0.4 % of the bulk velocity [Hirota *et al.* (1998)]. It is expected that these two flow-inlet conditions cover the usual extremes encountered in practical applications [Kays and Crawford (1980)].

Figure 3.2 shows the examples of distributions of the primary-flow velocity ( $U_1$ ) and turbulence intensity  $\sqrt{u_1^2}$  measured under these flow-inlet conditions. They were obtained in a straight rectangular channel, which has the same entrance configurations and cross-sectional dimension as adopted in this study, at a location  $8 d_h$  downstream of the entrance [Hirota *et al.* (1992)]. This measuring cross-section agrees nearly with the entrance of the turn section in the present test channels. The left half of Fig. 3.2 shows the distribution of  $U_1$  obtained in a half cross-section of the channel, and the right half shows that of  $\sqrt{u_1^2}$ ; they are made dimensionless by the bulk velocity  $U$ . Under the contracted-flow inlet condition shown in Fig. 3.2 (a), the turbulence intensity at the channel center is about 5 % of  $U$  and thus turbulent boundary layers are formed over the cross-section. On the other hand, under the uniform-flow inlet shown in Fig. 3.2 (b), the turbulent boundary layer can be observed only in the vicinity of the wall and thus the flow in the core region is in a laminar condition. These results suggest that the flow characteristics just before the turn section in the present serpentine channels can be also greatly influenced by the flow-inlet condition at the channel entrance.

Experiments were conducted in the Reynolds number range of turbulent flow,  $Re = (2.0-6.0)$

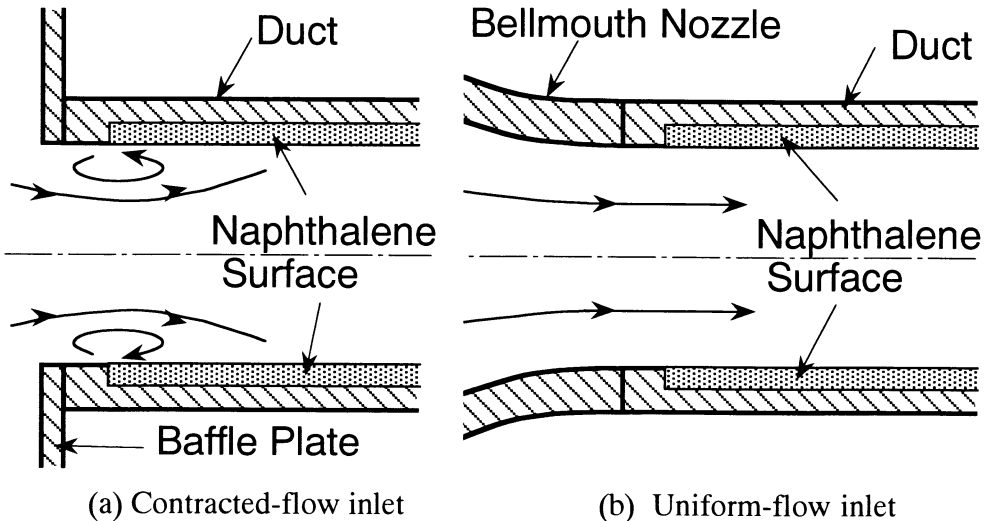
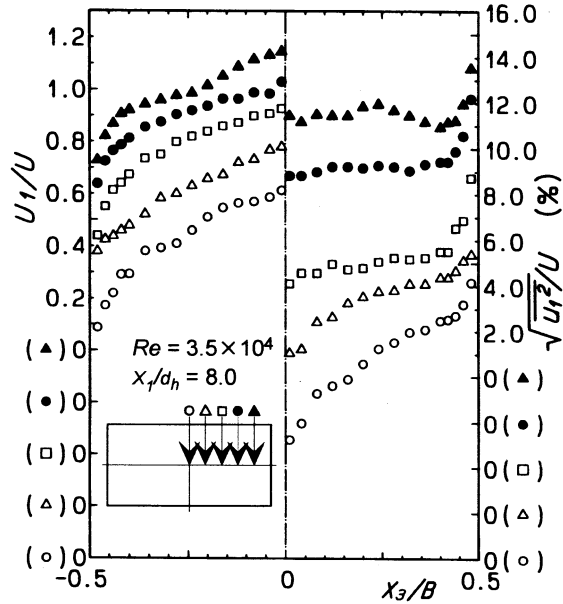
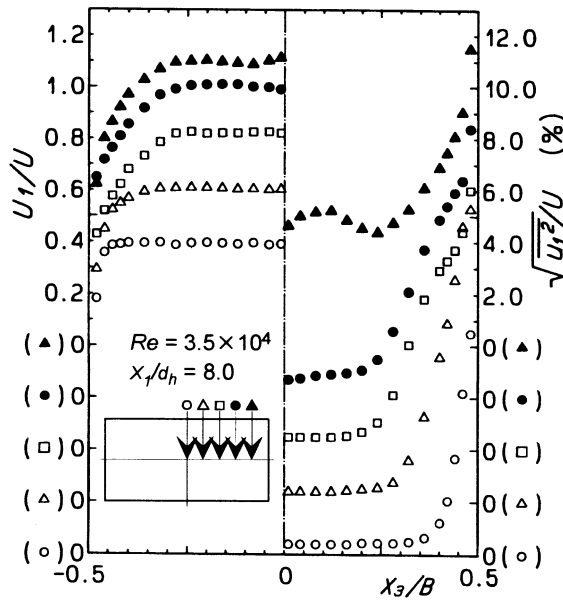


Fig. 3.1 Flow-inlet conditions at the duct entrance



(a) Contracted-flow inlet



(b) Uniform-flow inlet

Fig. 3.2 Distributions of primary-flow velocity (left half) and turbulence intensity (right half) measured at  $8.0 d_h$  downstream from the channel entrance

$\times 10^4$ . In this paper, however, the results obtained at a single  $Re$  of  $3.5 \times 10^4$  are presented. In addition to the mass-transfer experiment, we measured the pressure distributions along the spanwise centerline of the bottom wall. The locations of the pressure taps are the same as those shown in Chapter 2. The pressure measurements were also conducted for two more turn clearances of  $C = 40$  mm and 60 mm. As described later, in addition to the channels of 30 mm, 50 mm, and 70 mm in which the mass transfer was measured on all the channel walls, the mass transfer measurements on the bottom wall only were also conducted in the channels of  $C = 40$  mm and 60 mm.

### 3.3 Results of Experiments

#### 3.3.1 Pressure Distribution and Pressure Loss Coefficient

Figure 3.3 shows the pressure distributions obtained with a medium turn clearance of  $C = 50$  mm under various  $Re$ 's. The abscissa shows the pressure-tap number shown in Fig. 2.5, and the ordinate shows the dimensionless local pressure. Under the contracted-flow inlet shown in Fig. 3.3(a), the pressure shows the local minimum at Tap 0 because of the flow separation at the channel entrance. The pressure distribution for the uniform-flow inlet shown in Fig. 3.3(b) is qualitatively similar to that for the contracted-flow inlet, except that the local minimum at Tap 0 does not appear. Thus, it follows that the pressure distribution on the bottom wall does not reflect such difference of the flow characteristics as observed in Fig. 3.2 which is caused by the difference of the flow-inlet condition.

Next, the coefficient of pressure loss  $K$  defined by Eq. (3.1) has been calculated from the pressure distribution.

$$K = \frac{2\Delta P}{\rho U^2} \quad (3.1)$$

$\Delta P$  for the uniform-flow inlet is the pressure difference between Tap 1 and Tap 11. Definition of  $\Delta P$  for the contracted-flow inlet is described in Chapter 2. Figure 3.4 shows the variations of  $K$  against  $Re$ . The values of  $K$  for the contracted-flow inlet are about 20 % larger than those for the uniform-flow inlet, but qualitative characteristics of  $K$  are quite similar to each other.  $K$  is nearly constant against  $Re$ , and  $C$  is decisive for  $K$ -values. The values of  $K$  increase as the turn clearance is decreased, and those for  $C = 30$  mm are significantly larger than those for wider turn clearances.

#### 3.3.2 Mean Sherwood Number

Figure 3.5 (a) shows the variations of the mean Sherwood number  $Sh_m$  against  $Re$  obtained under the both flow-inlet conditions for a medium turn clearance  $C = 50$  mm. In this figure, the Sherwood numbers averaged in the upstream and downstream halves of the test channel, denoted as  $Sh_{mu}$  and  $Sh_{md}$  respectively, are also shown. The values of  $Sh_m$  for the contracted-flow inlet are about 1.2–1.3 times as large as those for the uniform-flow inlet. In particular,  $Sh_{mu}$  of the contracted-flow inlet is 1.5–1.9 times that of the uniform-flow inlet; such high values of  $Sh_{mu}$  reflect the mass transfer augmentation effect of the strong turbulence produced by the flow separation at the sharp-edged entrance.

Downstream of the turn,  $Sh_{md}$  for the contracted-flow inlet is also larger than that for the uniform-flow inlet at a low  $Re$ . This means that the influence of the flow-inlet condition on the mass transfer is maintained up to the region downstream of the turn. In the case of the sharp-edged inlet as well as the uniform-flow inlet,  $Sh_{md}$  is larger than  $Sh_{mu}$  and the same tendency was also observed in other turn clearances. Therefore it follows that, in the turn clearances tested in this study, the mass transfer augmentation effect of the sharp turn is larger than that of the sharp-edged entrance.

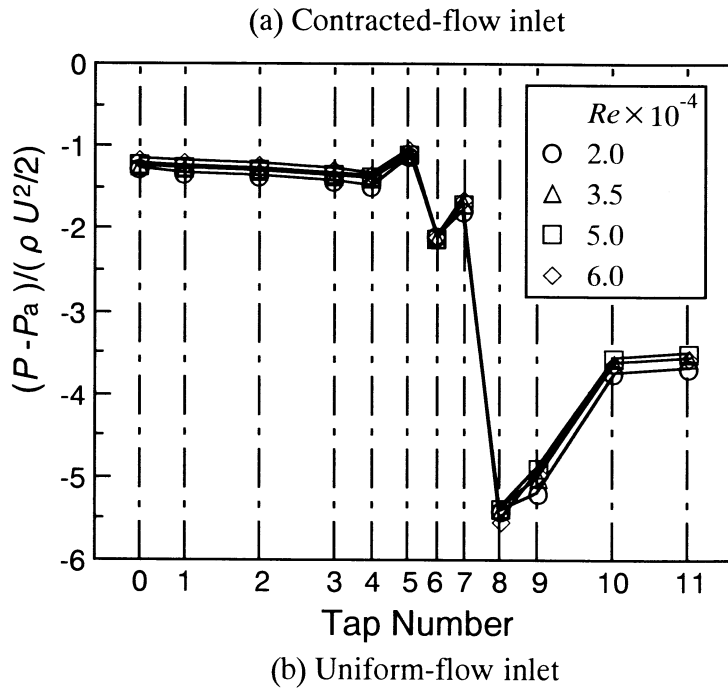
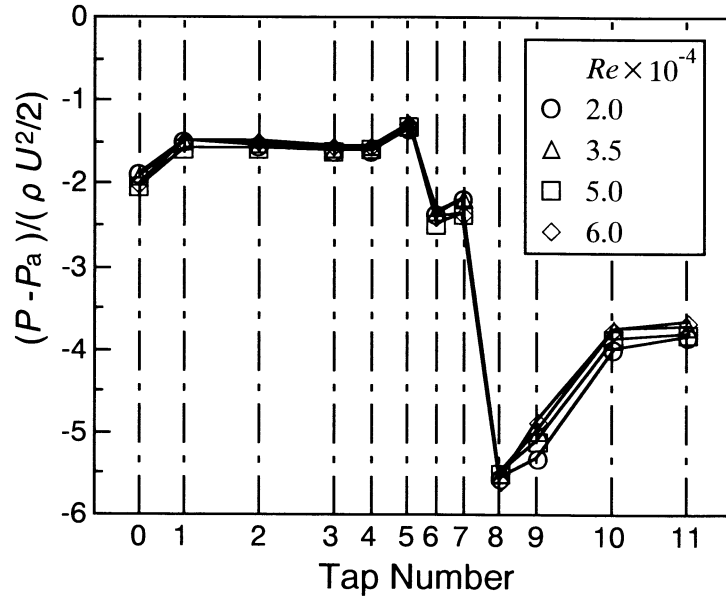
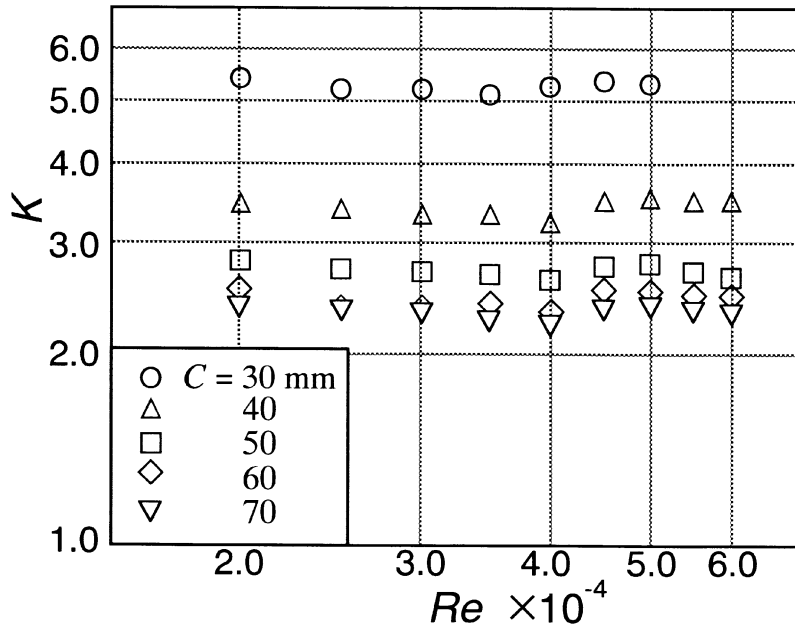
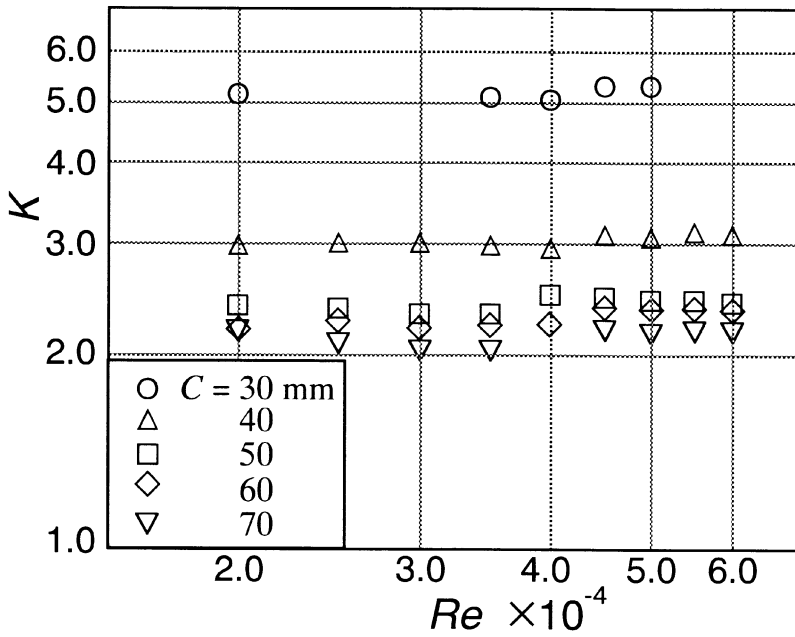


Fig. 3.3 Pressure distributions

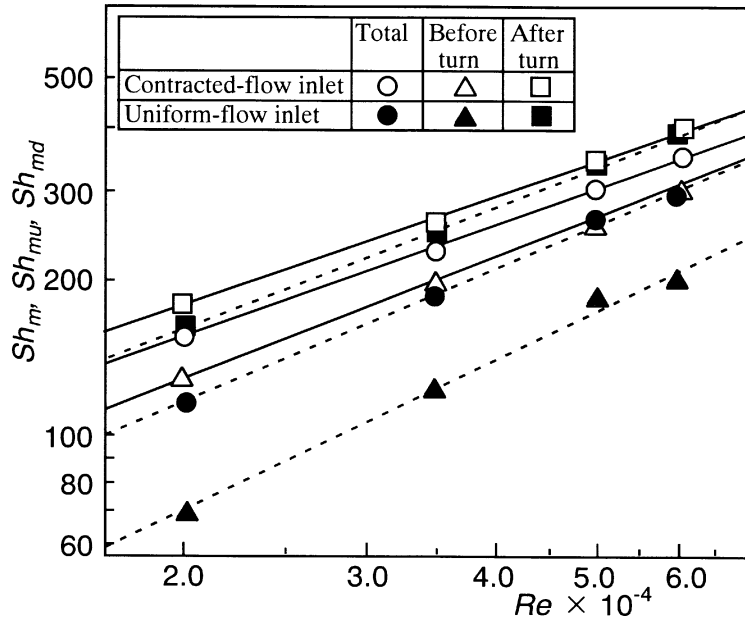


(a) Contracted-flow inlet

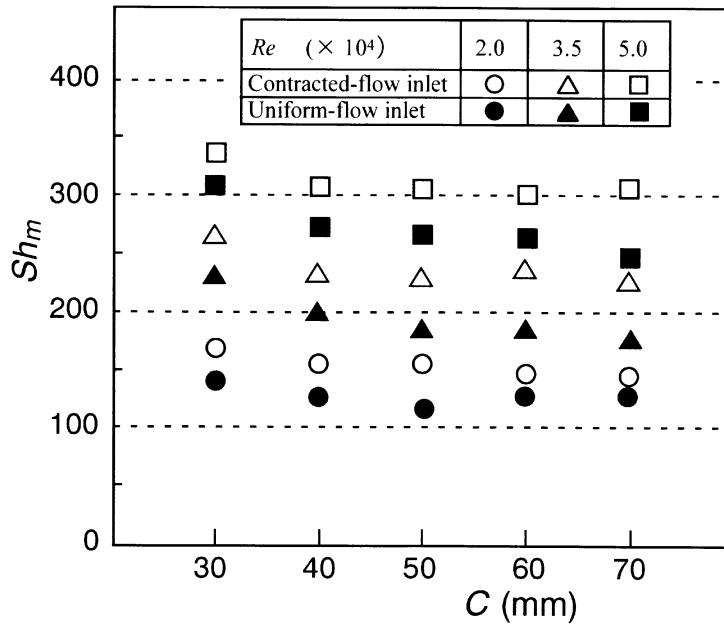


(b) Uniform-flow inlet

Fig. 3.4 Coefficients of pressure loss



(a) Variations of mean Sherwood numbers against  $Re$  ( $C = 50$  mm)



(b) Variations of mean Sherwood numbers against  $C$

Fig. 3.5 Mean Sherwood numbers

Figure 3.5 (b) shows the variations of  $Sh_m$  against the turn clearance  $C$ .  $Sh_m$  is almost independent of the turn clearance in the range of  $C = 40$  mm–70 mm, and  $Sh_m$ -values for  $C = 30$  mm are exceptionally larger than those for the larger turn clearances. From these results, it follows that  $Sh_m$  of the present test channels is more influenced by the flow-inlet condition than by the turn clearance.

### 3.3.3 Block-Averaged Sherwood Number

Similar to Chapter 2,  $Sh_B$  was obtained by dividing the test section into 14 blocks as shown in Fig. 2.10, and by calculating the integral average of the local Sherwood number in them on each wall (see Eq. (2.4) for definition). Figure 3.6 shows the distributions of  $Sh_B$  obtained in the channel of largest turn clearance  $C = 70$  mm; the abscissa in the figure shows the block-number defined in Fig. 2.10.

The distributions of  $Sh_B$  on the bottom wall are shown in Fig. 3.6 (a). Under the contracted-flow inlet (shown by the symbol “○”),  $Sh_B$  shows the maximum in Block 1, then decreases in the flow direction due to the development of the concentration boundary layer, and reaches the minimum in Block 5.  $Sh_B$  then increases in Blocks 7 and 8, i. e., in the turn section, and attains the local maximum in Block 10 that is located downstream of the turn section. After Block 10,  $Sh_B$  decreases in the flow direction but increases again in Block 14 due to the influence of the sharp turn located at the end of the test section.

Under the uniform-flow inlet [shown by “△” in Fig. 3.6 (a)],  $Sh_B$  shows the local maximum at Block 1 but its value is considerably smaller than that for the contracted-flow inlet. After  $Sh_B$  shows the minimum in Block 2 (this location is different from that for the contracted-flow inlet), it increases in the flow direction to reach the maximum in Block 10. On the bottom wall, the difference in the  $Sh_B$  distributions due to the flow-inlet condition is observed rather obviously in Blocks 1 to 6. Even in Blocks 7 and 8, i. e., in the turn section,  $Sh_B$  for the uniform-flow inlet is somewhat smaller than that for the contracted-flow inlet, thus it follows that the influence of the flow-inlet condition on  $Sh_B$  appears in the turn section as well.

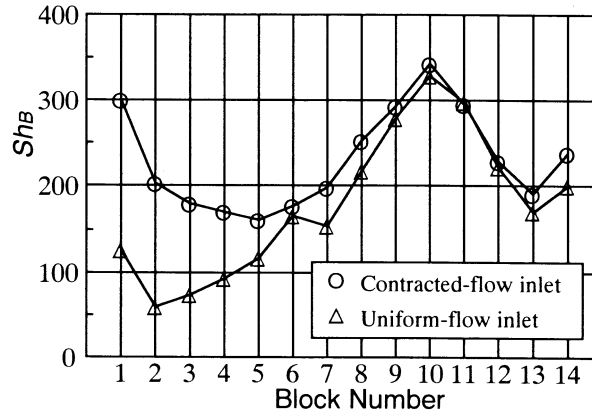
Figures 3.6 (b) and 3.6 (c) show the  $Sh_B$  distributions on the outer wall [walls (i), (iii), and (v) in Fig. 2.2] and those on the inner wall [walls (ii) and (iv)], respectively. It should be noted that, in Fig. 3.6(b), Blocks 7 and 8 are located on the outer walls (i) and (v), respectively, and Blocks 7e and 8e are on the end wall [wall (iii)]. The influence of the flow-inlet condition is observed clearly in the  $Sh_B$  distribution near the channel entrance of Blocks 1 and 2, but it once disappears in Blocks 3 to 6. In and after the turn section (Blocks 7 to 14), however, the influence of the flow-inlet condition on  $Sh_B$  emerges again;  $Sh_B$  for the contracted-flow inlet is remarkably larger than that for the uniform-flow inlet. It follows that, in the region after the turn (Blocks 9 to 14), the  $Sh_B$  distributions on the short-side walls reflect the flow-inlet conditions more distinctly than those on the long-side wall.

### 3.3.4 Distribution of Local Sherwood Number

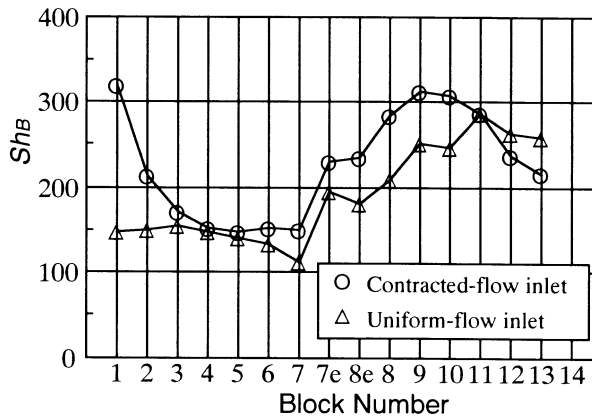
In this section, similar to Chapter 2, the distributions of the local Sherwood number  $Sh = h_m d_h / D$  are presented in the form of 2-D maps (Figs. 3.7 to 3.12). We also present the specially magnified detail maps showing the  $Sh$  distribution around the turn section (bottom wall only). The characteristics of  $Sh$  distributions for each turn clearance are described below.

#### (1) Channel with $C = 30$ mm

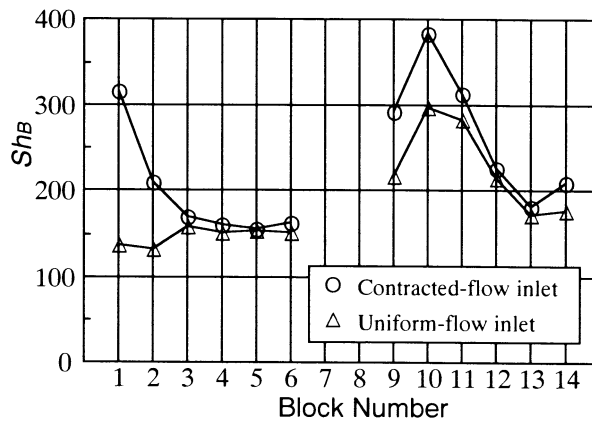
Figures 3.7 (a) and 3.7 (b) show the  $Sh$  distributions obtained in the channel with the narrowest turn clearance  $C = 30$  mm under the contracted-flow inlet and the uniform-flow inlet conditions, respectively. Details in the turn section on the bottom wall [wall (vi)] are shown in Fig. 3.8. The characteristics of  $Sh$  distributions are described below by dividing the whole test section into three parts; (a) straight section before the turn (b) turn section, and (c) straight section after the



(a) Bottom wall



(b) Outer wall



(c) Inner wall

Fig. 3.6 Comparison of Block-averaged Sherwood numbers ( $C = 70$  mm)

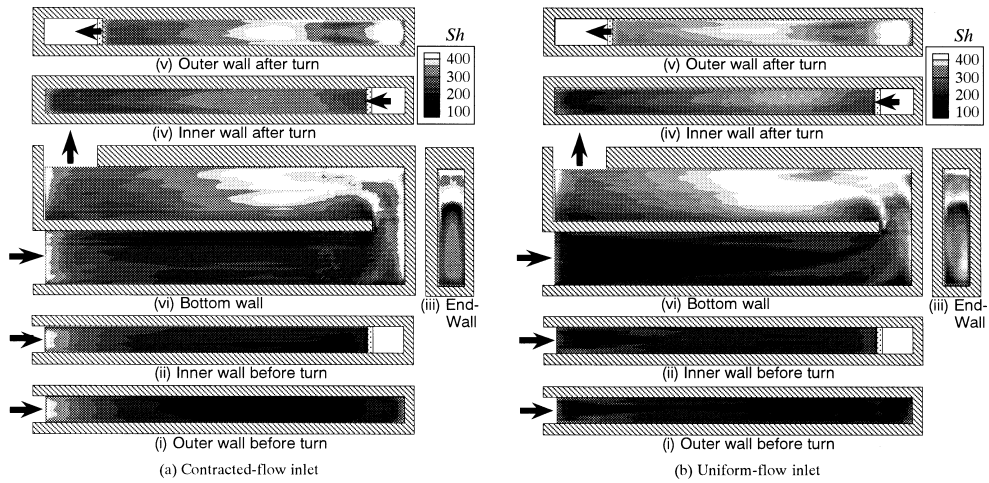


Fig. 3.7 Distributions of local Sherwood number ( $C = 30$  mm)

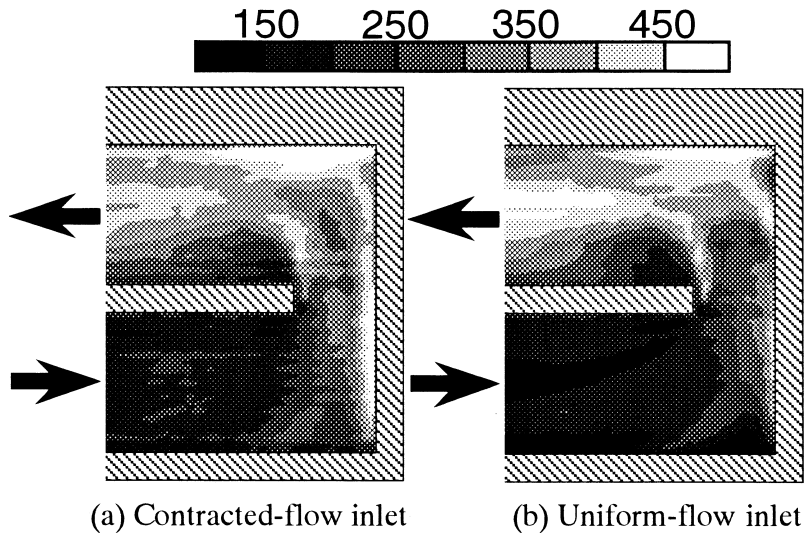


Fig. 3.8 Details of local Sherwood number around the turn ( $C = 30$  mm)  
left; Contracted-flow inlet, right; Uniform-flow inlet

turn.

(a) *Straight section before the turn (Blocks 1 to 6)* Under the contracted-flow inlet condition [Fig. 3.7 (a)],  $Sh$  shows the local maximum at the entrance and decreases as the flow proceeds downstream; very large values of  $Sh$  are caused near the entrance by the strong turbulence produced in the shear layer of the separated flow and by the leading-edge effect of the concentration

boundary layer.  $Sh$  shows quite uniform distributions in the spanwise direction on all the walls.

On the other hand, under the uniform-flow inlet condition shown in Fig. 3.7 (b), the triangular-shaped low  $Sh$  regions are observed on all the walls in the straight section before the turn. In the preceding experiment on the developing mass transfer in a straight rectangular channel, it was found that a laminar boundary layer first developed near the entrance and its transition to turbulent one initiated from the channel corner [Hirota et al. (1998b)]. The transitional region with higher mass transfer rates then developed toward the core region as the flow proceeded downstream, and consequently a triangular-shaped laminar mass transfer region of low mass transfer rates remained on the channel wall. The triangular-shaped low  $Sh$  region in Fig. 3.7 (b) corresponds to such laminar mass transfer region. On the bottom wall shown in (vi), the apex of this triangular region deviates from the spanwise centerline toward the inner-wall side near the entrance of the turn section (in Block 6). This suggests that the influence of the turn on the flow field already appears in the region upstream of the turn.

On the outer and inner walls [(i) and (ii)], the triangular shaped low  $Sh$  region disappears at the more upstream location, around Block 2, than that on the bottom wall. This is explained as follows. Because the spanwise length of the inner and outer walls (short-side walls) is just the half of that of the bottom wall (long-side wall), the transitional regions on the former walls [(i) and (ii)] developing from the corners reach the spanwise centerlines of those walls earlier than that on the bottom wall. Thus, the laminar mass transfer regions on the short-side walls disappear around Block 2 located relatively near the entrance. The influence of this earlier transition can be also observed in the distributions of the block-averaged Sherwood numbers  $Sh_B$  on the short-side walls shown in Figs. 3.6 (b) and 3.6 (c). That is, no significant influence of the flow-inlet condition can be observed in Blocks 3 to 6 which correspond to the transitional region on the short-side walls.

**(b) Turn section (Blocks 7 and 8)** In the turn section, the qualitative characteristics of  $Sh$  distributions for the contracted-flow inlet mostly agree with those for the uniform-flow inlet. Since the detailed characteristics of local mass transfer in the turn section were already described in Chapter 2, only the influence of the flow-inlet condition on the  $Sh$  distributions in the turn section is examined here based on Figs. 3.8 (a) and 3.8 (b).

In the upstream half of the turn section,  $Sh$  distribution for the contracted-flow inlet agrees qualitatively well with that for the uniform-flow inlet, but the  $Sh$ -values for the uniform-flow inlet are generally smaller than those for the contracted-flow inlet. Such quantitative difference in  $Sh$ -values is observed distinctly in the region near the junction with the end wall in which  $Sh$  attains the local maximum; the high  $Sh$  region of  $Sh > 450$  (white region) for the contracted-flow inlet appears in a larger area than that for the uniform-flow inlet. Moreover, near the corner in Block 7 under the uniform-flow inlet, the low  $Sh$  region corresponding to the recirculation zone appears more clearly and  $Sh$ -values in it is smaller than that for the contracted-flow inlet. In the downstream half of the turn section, the values of  $Sh$  for the uniform-flow inlet are also lower than those for the contracted-flow inlet, but such difference in  $Sh$ -values seems to be rather small compared to that observed in the upstream half.

**(c) Straight section after the turn (Blocks 9 to 14)** Under both flow-inlet conditions, as observed in Fig. 3.7, the low mass transfer region is formed near the inner-wall tip (in Block 9), and  $Sh$  attains the local maximum in Block 10. In Block 10, the values of  $Sh$  on the outer wall [wall (v)] are much larger than those on the inner wall [wall (iv)]; moreover, on the bottom wall, the high  $Sh$  region deviates to the outer-wall side. These results clearly show that, irrespective of the flow-inlet condition, the flow which is separated at the inner-wall tip forms a separation bubble along the inner wall and reattaches in Block 10 on the outer wall. After the flow reattachment, the deflection of the high  $Sh$  region to the outer-wall side is observed up to the end of the test section.

There appears very little difference between the  $Sh$  distributions for the contracted-flow inlet and the uniform-flow inlet in the section after the turn. Therefore, it follows that, in the channel

with a narrow turn clearance, the influence of the flow-inlet condition on the local mass transfer characteristics diminishes to a large extent after the flow passes through the turn clearance. A close comparison of  $Sh$ -values in Block 10 on the outer wall in Fig. 3.7 (a) and Fig. 3.7 (b), however, reveals that the  $Sh$ -values around the flow-reattachment point for the former (contracted-flow inlet) are slightly larger than that for the latter (uniform-flow inlet). This suggests that the flow characteristics near the exit of the turn section are rather sensitive to the flow-inlet condition.

(2) **Channel with  $C = 50$  mm**

Next, the  $Sh$  distributions in the channel with a medium turn clearance of  $C = 50$  mm, which is just the same as the spanwise length of the long-side wall, are shown in Figs. 3.9 (overall view) and 3.10 (turn section). The  $Sh$  distributions in the straight section before the turn are qualitatively and quantitatively similar to those in the channel with  $C = 30$  mm; namely, in Fig. 3.9 (b), the triangular-shaped low  $Sh$  regions which are peculiar to the uniform-flow inlet are observed on all the walls.

In the upstream half of the turn section (Block 7) also,  $Sh$  distributions in the present channel show the qualitatively similar characteristics as those in the channel with  $C = 30$  mm. That is, the values of  $Sh$  obtained under the uniform-flow inlet condition are somewhat smaller than those for the contracted-flow inlet, and this tendency can be observed most distinctly in the recirculation zone near the upstream corner in the turn section and in the high  $Sh$  region on the bottom wall near the junction with the end wall.

In the downstream half of the turn section (Block 8),  $Sh$ -values are smaller than those for the channel with  $C = 30$  mm under both flow-inlet conditions. This decrease in  $Sh$ -values in the present channel is especially pronounced on the outer wall [wall (v)]. This is explained by the decrease of flow velocity that impinges on this wall after passing through a wider turn clearance. From Fig. 3.10, it is also found that  $Sh$ -values for the uniform-flow inlet are smaller than those for the contracted-flow inlet in not only the upstream half but also the downstream half of the turn section. In particular, a detailed comparison of Fig. 3.8 and Fig. 3.10 reveals that, in the downstream half of the turn section, the influence of the flow-inlet condition on  $Sh$  distribution appears more clearly in the present channel than the case of the narrower turn clearance of  $C = 30$  mm.

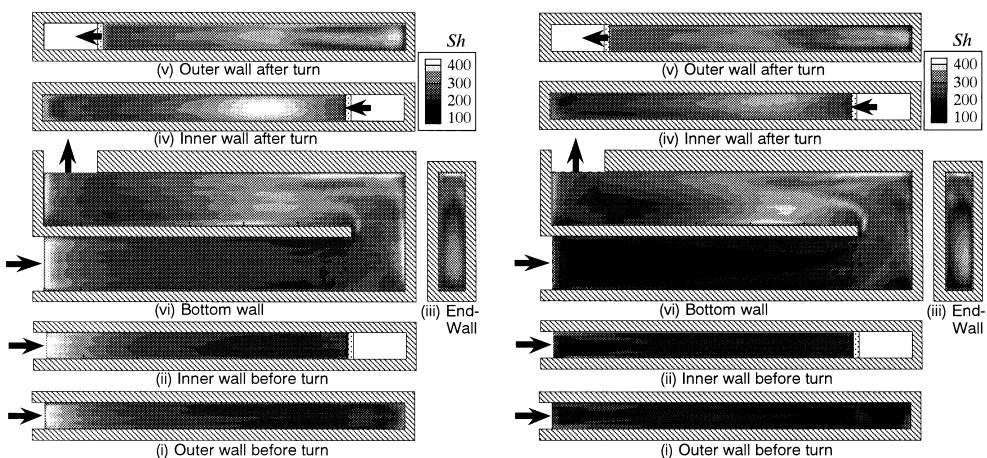


Fig. 3.9 Distributions of local Sherwood number ( $C = 50$  mm)

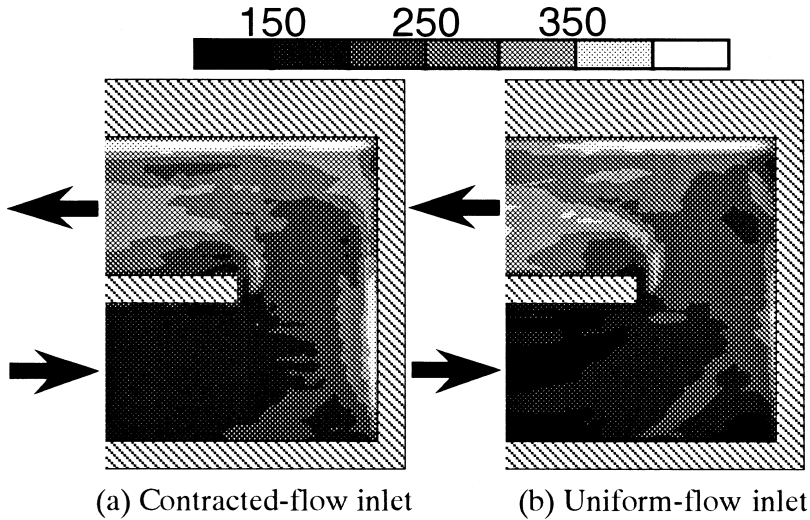


Fig. 3.10 Details of local Sherwood number around the turn ( $C = 50$  mm)  
left; Contracted-flow inlet, right; Uniform-flow inlet

The flow that exits the turn section is separated at the inner-wall tip, as similar to the case of  $C = 30$  mm, and the low  $Sh$  region corresponding to the separation bubble is formed along the partition (inner) wall just after the turn in Block 9 under both flow-inlet conditions. In Block 10,  $Sh$  attains the local maximum on all the walls. The influence of the flow-inlet condition on the local mass transfer characteristics can be observed in Block 10 on the short-side walls as follows. Under the contracted-flow inlet shown in Fig. 3.9 (a),  $Sh$ -values on the inner wall [wall (iv)] are larger than those on the outer wall [wall (v)] if compared at the same streamwise location in the block. This means that, under the contracted-flow inlet, the flow separated at the inner-wall tip reattaches on the inner wall. On the other hand, in case of the uniform-flow inlet [Fig. 3.9 (b)],  $Sh$  in Block 10 on the inner wall is almost in the same values as that on the outer wall. Therefore, in this case, the short-side wall on which the separated flow reattaches can not be specified so clearly from the  $Sh$  distributions. These results show that, in the present channel with a medium turn clearance  $C = 50$  mm, the influence of the flow-inlet condition on the local mass transfer is still maintained in the region after the turn. It is thought that the flow separation and reattachment around the inner-wall tip have unsteadiness in nature, and that such unsteadiness in the flow characteristics may be intensified under the uniform-flow inlet relative to the case of contracted-flow inlet. This means that, under the uniform-flow inlet, the flow separated at the inner-wall tip reattaches on both the inner wall and outer wall alternately, and consequently  $Sh$ -values on the outer wall become as large as those on the inner wall in Block 10.

On the bottom wall, the  $Sh$  distributions in Block 10 show quite a different tendency from those on the short-side walls. Under the contracted-flow inlet, the region of high  $Sh$ -values occupies most part of Block 10 and spanwise variations of  $Sh$  are not observed so clearly; whereas, under the uniform-flow inlet, the high  $Sh$  region is deviated to the inner-wall side. These characteristics of  $Sh$  distributions on the bottom wall are just opposite to those expected from the results on the short-side walls. This suggests that the mechanism of mass transfer enhancement in Block 10 on the short-side walls is different from that on the long-side wall. The high mass transfer rates on the short-side walls are mostly caused by the reattachment of the flow that is separated at the in-

ner-wall tip. The mechanism of the mass transfer enhancement on the bottom wall is not so clear at the present stage of the study. It may be possible that some longitudinal vortices that are formed after the turn section and are rotating in the direction opposite to the turn-induced Dean vortices [Mochizuki *et al.* (1998)] contribute to the mass transfer from the bottom wall.

After Block 11,  $Sh$  decreases gradually in the flow direction. A detailed comparison of  $Sh$  distributions obtained at an equal streamwise location reveals that  $Sh$ -values in the outer-wall side are larger than those in the inner-wall side. Such spanwise non-uniformity of  $Sh$  distribution after the turn appears more obviously under the uniform-flow inlet than the contracted-flow inlet. From a comparison of the present results with those for  $C = 30$  mm, it is found that the influence of the flow-inlet condition on  $Sh$  distribution is maintained over a longer distance after the turn in the present channel with a larger turn clearance. The reason will be described later in Section 3.4.

### (3) Channel with $C = 70$ mm

$Sh$  distributions in the channel with the largest turn clearance of  $C = 70$  mm are shown in Figs. 3.11 and 3.12. The distributions of  $Sh$  in the straight section before the turn agree well with those in other channels with smaller turn clearance described above. In the upstream half of the turn section (Block 7), the low  $Sh$  region near the corner is observed more clearly than that in the other channels with smaller  $C$ . Moreover, the tendency that this low  $Sh$  region under the uniform-flow inlet occupies larger area on the bottom wall than that for the contracted-flow inlet is most pronounced in the present channel.

In the downstream half of the turn section, because of the deceleration of the flow in passing through the larger turn clearance and resultant decrease of the flow velocity reversing to the end wall,  $Sh$  shows the local minimum in the downstream edge of the end wall. This local minimum on the end wall of the present channel is just opposite to the local maximum observed in the other channels. It is recognized from a comparison of Fig. 3.12 (a) with Fig. 3.12 (b) that, as similar to the other channels,  $Sh$  for the uniform-flow inlet shows smaller values than that for the contracted-flow inlet. It is also found that this tendency appears more clearly in the present channel than the case of smaller turn clearances.

In the straight section after the turn, the characteristics of  $Sh$  distributions in the present channel

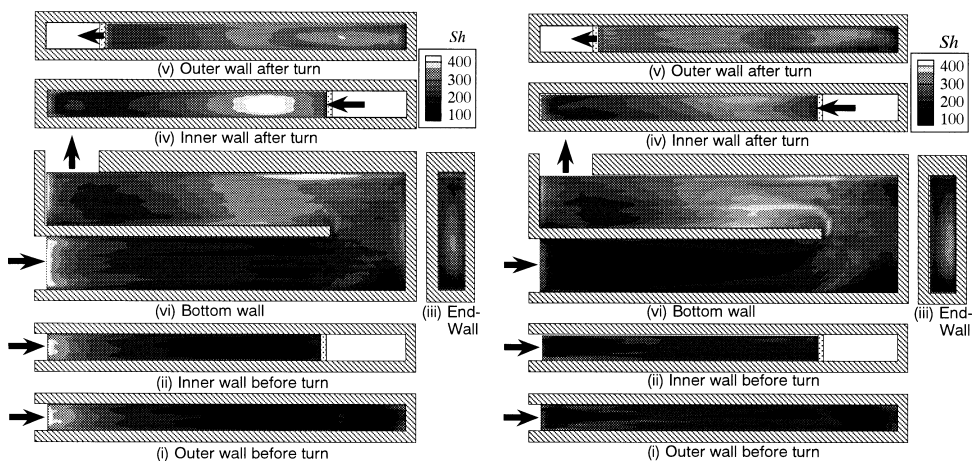


Fig. 3.11 Distributions of local Sherwood number ( $C = 70$  mm)

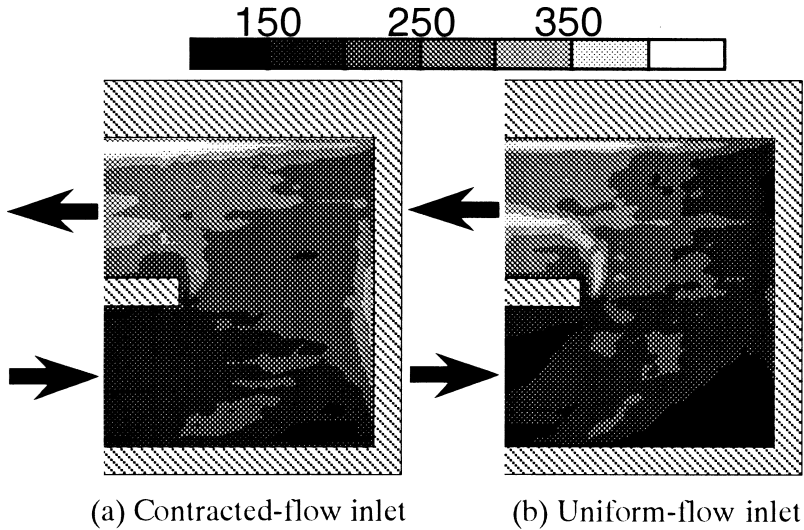


Fig. 3.12 Details of local Sherwood number around the turn ( $C = 70$  mm)  
left; Contracted-flow inlet, right; Uniform-flow inlet

are quite similar to those in the channel with  $C = 50$  mm. After the low  $Sh$  region that corresponds to the separation bubble formed along the partition (inner) wall,  $Sh$  reaches the local maximum in Block 10. The influence of the flow-inlet condition on the  $Sh$  distributions, which is similar to that observed in the channel with  $C = 50$  mm, is clearly observed there. That is, under the contracted-flow inlet the  $Sh$ -values on the inner wall are larger than those on the outer wall, while in case of uniform-flow inlet  $Sh$  in Block 10 on the inner wall is almost the same values as that on the outer wall. Moreover, the  $Sh$  distributions in Block 10 on the bottom wall are inconsistent with those on the short-side walls. From a comparison of Fig. 3.7, Fig. 3.9 and Fig. 3.11, it can be concluded that, as the turn clearance is increased, the flow-inlet condition tends to exert greater influence on the mass transfer characteristics in and after the turn section.

### 3.4 Discussion

As have been described so far, in the rectangular serpentine channels with relatively short flow passages tested here, the flow-inlet condition at the entrance exerts considerable influence on the local mass transfer characteristics in the whole regions of the channel. After the turn section, however, such influence becomes weaker as the turn clearance is decreased. The reason for such tendency can be qualitatively explained as follows.

In general, fluid lumps in the core region just before the turn section are convected to the vicinity of the channel walls after the turn by the secondary flow that arises in the turn. As shown in Fig. 3.2, in the flow near the entrance of the turn section for the uniform-flow inlet, turbulence is restricted in narrow regions near the channel walls and the core region is still in a laminar flow condition. On the other hand, under the contracted-flow inlet, higher turbulence intensity can be observed in the whole cross-section and thus the flow is in a fully turbulent condition. Therefore, the turbulence intensity in the fluid lumps which are convected to the vicinity of the walls after the turn by the secondary flow changes considerably depending on the flow-inlet condition at the channel entrance. This change in the turbulence intensity then influences the local mass transfer after

the turn, and causes such difference of  $Sh$  distributions due to the flow-inlet condition as described above.

In the channel with a narrow turn clearance, the flow velocity increases in passing through the turn clearance and large production of turbulence occurs around the inner-wall tip. As a result, at the exit of the turn section, there exists strong turbulence over the whole channel cross-section and it dominates the mass transfer after the turn. Therefore, the influence of the turbulence existing before the turn on the local mass transfer after the turn becomes relatively weak, and consequently the  $Sh$  distribution after the turn becomes less sensitive to the flow-inlet condition than the case of the larger turn clearance.

### 3.5 Conclusions

In this chapter, the influence of the flow-inlet condition at the channel entrance on the local heat (mass) transfer characteristics in the channels has been examined. Two contrastive flow-inlet conditions, contracted-flow inlet and uniform-flow inlet, have been tested for three turn clearances. Main results are summarized as follows.

(1) In the straight section before the turn, the influence of the flow-inlet condition on the local Sherwood number ( $Sh$ ) distributions appears very clearly. Under the uniform-flow inlet, the triangular shaped low  $Sh$  region corresponding to the laminar mass transfer appears on all the walls. On the other hand, under the contracted-flow inlet, such a laminar mass transfer region does not appear at all, and  $Sh$  shows quite uniform distributions in the spanwise direction.

(2) In the upstream half of the turn section, under both flow-inlet conditions,  $Sh$  attains the local maximums on the end wall and on the bottom wall near the junction with the end wall, while a low  $Sh$  region corresponding to the recirculation zone appears near the corner. The  $Sh$ -values for the uniform-flow inlet are somewhat smaller than those for the contracted-flow inlet irrespective of the turn clearance.

(3) In the downstream half of the turn section, the qualitative characteristics of the  $Sh$  distribution do not change so distinctly depending on the flow-inlet condition. The  $Sh$ -values for the uniform-flow inlet are, however, generally smaller than those for the contracted-flow inlet; this tendency appears more clearly in the channels with a larger turn clearance.

(4) In the straight section after the turn with a larger turn clearance, the influence of the flow-inlet condition appears most distinctly in the  $Sh$  distributions around the flow-reattachment point (Block 10). Under the contracted-flow inlet,  $Sh$  on the inner wall shows higher values than that on the outer wall. On the other hand, under the uniform-flow inlet, there appears very little difference between the  $Sh$ -values on the inner wall and outer wall. As the turn clearance is decreased, however, such influence of the flow-inlet condition on the  $Sh$  distributions in Block 10 becomes weaker.

(5) In Block 10, the characteristics of  $Sh$  distribution on the bottom wall are inconsistent with those on the short-side walls. That is, under the contracted-flow inlet the entire area of Block 10 is occupied by a high  $Sh$  region and no spanwise variations appear in the  $Sh$  distribution, whereas under the uniform-flow inlet the high  $Sh$  region tends to deviate toward the inner-wall side. Such characteristics of  $Sh$  distributions on the bottom wall are just opposite to those expected from the results on the short-side walls described above in (4).

#### 4. Influence of Inclination Angle of Partition (Inner) Wall

##### 4.1 Introduction

As described in Chapter 2 and Chapter 3, the local heat (mass) transfer rates in the rectangular channels with a sharp 180-degree turn change very steeply in and after the turn section, and the non-uniformity of their distributions becomes quite large there. The non-uniform distribution of the local heat transfer rates causes large temperature gradients and consequently increases the thermal stress. Therefore, in applying those serpentine channels to practical equipment used under severe thermal conditions, it is important not only to enhance the heat transfer but also to increase the uniformity in the distributions of the local heat transfer rates. In most studies conducted to date, however, only the enhancement of heat transfer was studied intensively and no attention was directed to the improvement of the uniformity in the distribution of local heat transfer rates.

Hence, in this study, we have made an attempt to enhance the overall heat transfer rate and concurrently to improve the uniformity of the local Nusselt (Sherwood) number distributions in the serpentine channel with a sharp turn [Hirota et al. (1999c)]. As a means to accomplish this purpose, we have tested the “inclined partition (inner) wall” (see Fig. 4.1). By inclining the inner wall with respect to the outer walls, the primary flow in the convergent (or divergent) sections before and after the turn is accelerated (or decelerated) due to the streamwise change of the channel cross-sectional area. The influence of such acceleration or deceleration of the primary flow can be then reflected on both the distributions of the secondary flow velocities and the characteristics of flow separation and reattachment around the turn section. As a result, the local heat transfer characteristics in the channel may be considerably altered from those in the standard parallel-walled channel. It can be expected that, by selecting some optimum condition of the inclination angle, both the improvement of the local heat transfer uniformity and the enhancement of the mean heat transfer be achieved concurrently without a considerable increase in the pressure loss.

In this chapter, we show the results of an experimental study on heat (mass) transfer in rectan-

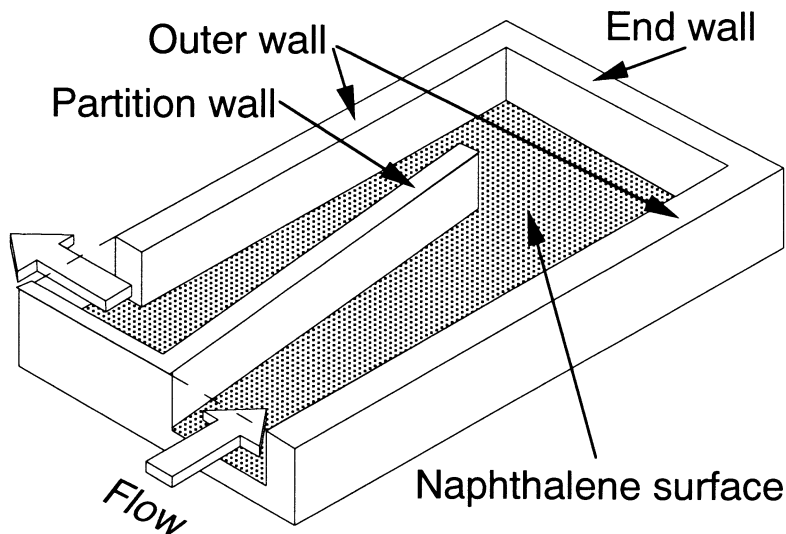


Fig. 4.1 Test section

gular cross-sectioned serpentine channels with an inclined partition wall. As the first step of the project, we have measured mass transfer rates on the long-side wall of the channel only (see Fig. 4.1) to elucidate whether or not this inclined partition wall is effective to the enhancement of heat transfer and/or the improvement of the heat transfer uniformity. Six inclination angles were tested for three turn clearances under a single Reynolds number. In this chapter, the detailed results of heat transfer obtained in the channels are shown and, based on the experimental results, the optimum combination of the inclination angle and the turn clearance that can achieve both the enhancement of heat transfer and the improvement of heat transfer uniformity is examined.

#### 4.2 Experimental Apparatus and Procedure

The flow loop is essentially the same as that used in the preceding experiments described in Chapters 2 and 3. A schematic illustration of the test section is shown in Fig. 4.1. The test channel has a rectangular cross-section; the short-side length is 25 mm and is constant throughout the test section, while the long-side length is 50 mm at the channel entrance and varies in the flow direction depending on the inclination angle of the inner wall. The hydraulic diameter defined at the entrance of the channel,  $d_h$ , is 33.3 mm. As shown in Fig. 4.1, the surface of one long-side wall was coated by naphthalene, and the local mass transfer rates on it were measured. The other long-side wall and all short-side walls were made of smooth aluminum plates, corresponding to the adiabatic thermal condition.

Figure 4.2 shows the details of the naphthalene surface in the mass transfer test section. The partition (inner) wall which divides the test section into two-pass passages is made of a smooth aluminum plate with 10 mm thick. The inclination angle of this partition wall, denoted as  $\alpha$  in the figure, was changed from  $-6^\circ$  (clockwise direction in the figure) to  $+6^\circ$  (counter-clockwise direction) at  $2^\circ$  intervals; totally six inclination angles except for  $\alpha = 0^\circ$  were tested in the present study. In this paper, the channels with  $\alpha < 0^\circ$  are called “convergent channels”, and those with  $\alpha > 0^\circ$  are called “divergent channels.” The channels with  $\alpha = 0^\circ$  having a parallel partition wall are called “standard channels”; they are same as the channels used in the preceding experiments described in Chapters 2 and 3. The turn clearance, denoted as  $C$  in Fig. 4.2, was varied from 30 mm to 70 mm at 20 mm pitch. The edge of the partition-wall tip is parallel to the end wall.

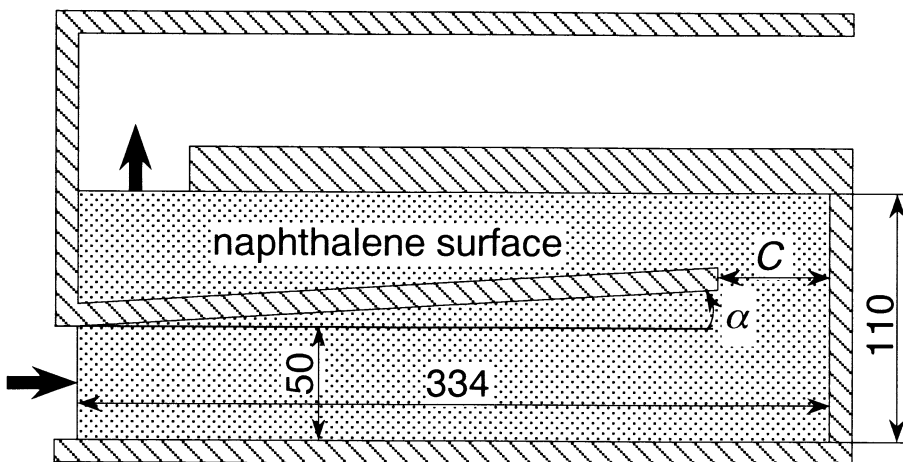


Fig. 4.2 Details of mass transfer surface

The measurement procedure of mass transfer coefficients by the naphthalene sublimation method is the same as that of the preceding experiment. The present study was conducted under the contracted-flow inlet condition, which is the same as that described in Chapters 2 and 3. The experiments were conducted under a single Reynolds number  $Re = Ud_h/\nu = 3.5 \times 10^4$ , which was defined by the bulk velocity and hydraulic diameter at the channel entrance.

### 4.3 Results and Discussion

#### 4.3.1 Mean Sherwood Number and Pressure Loss

Figure 4.3 shows the variation of the mean Sherwood number  $Sh_m$  against the inclination angle of the partition wall  $\alpha$  obtained for all turn clearances. Here, it should be noted that the present  $Sh_m$  was calculated based on the mass transfer rate averaged over the bottom wall, not all channel walls; thus its definition is different from that of  $Sh_m$  presented in Chapters 2 and 3. In the channels of  $\alpha < 0^\circ$ , i. e., in the convergent channel,  $Sh_m$  increases in proportional to the inclination of the partition wall for all turn clearances, and  $Sh_m$  for  $\alpha = -6^\circ$  is about 20 %–30 % larger than that for the standard channel with a parallel partition wall ( $\alpha = 0^\circ$ ). On the other hand, in the divergent channel of  $\alpha > 0^\circ$ ,  $Sh_m$  is almost constant against  $\alpha$  for  $C = 50$  mm and 70 mm and it decreases with  $\alpha$  for  $C = 30$  mm. In general,  $Sh_m$  shows higher values as the turn clearance  $C$  is decreased. The dependence of  $Sh_m$  on the turn clearance, however, is rather weak in the divergent channels and, in the channels of  $\alpha = 4^\circ$  and  $6^\circ$ ,  $Sh_m$ -values for different  $C$  agree one another irrespective of the turn clearance.

The coefficient of flow resistance  $K$  defined by Eq. (2.1) was also obtained by measuring the pressure distribution, and the result is shown in Fig. 4.4. In both the convergent channels and the divergent channels,  $K$  increases as the inclination of the partition wall (absolute value of  $\alpha$ ) is increased or as the turn clearance is decreased. Similar to the case of the standard channel described in Chapters 2 and 3,  $K$  for  $C = 30$  mm are significantly larger than those for wider turn clearances in the divergent and the convergent channels as well. However, such a difference in  $K$ -values caused by  $C$  becomes smaller in the divergent channels; this tendency is quite similar to  $Sh_m$ .

A comparison of  $Sh_m$  with  $K$  shown above leads to a conclusion that, from a viewpoint of a

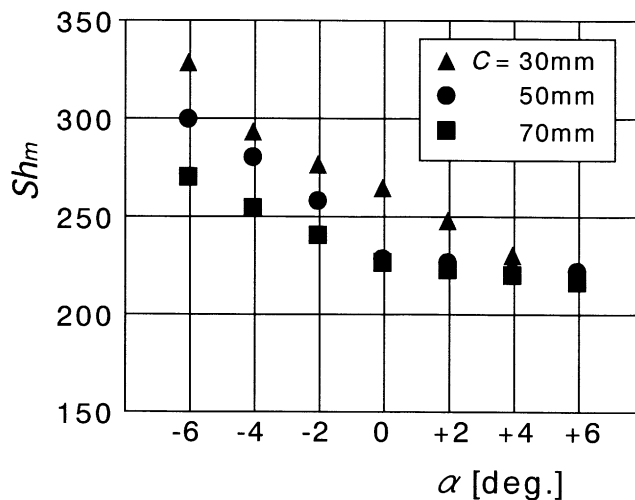


Fig. 4.3 Mean Sherwood numbers ( $Re = 3.5 \times 10^4$ ,  $C = 50$  mm)

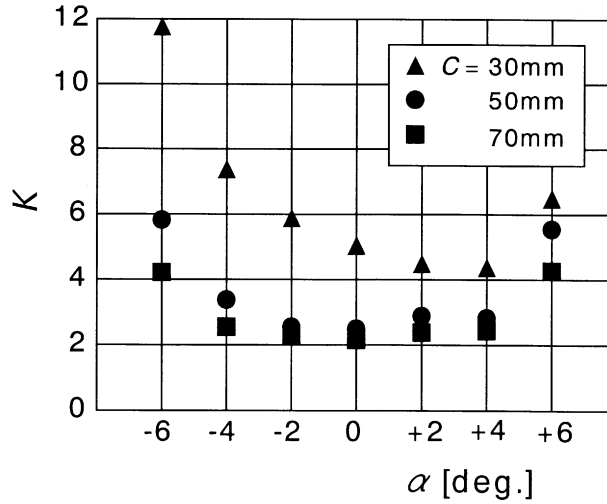


Fig. 4.4 Coefficient of flow resistance ( $Re = 3.5 \times 10^4$ ,  $C = 50$  mm)

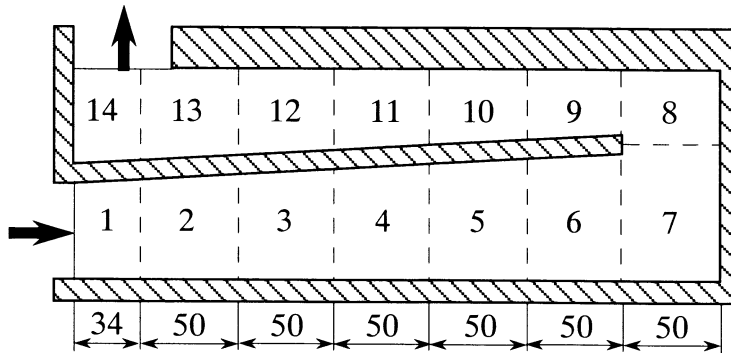
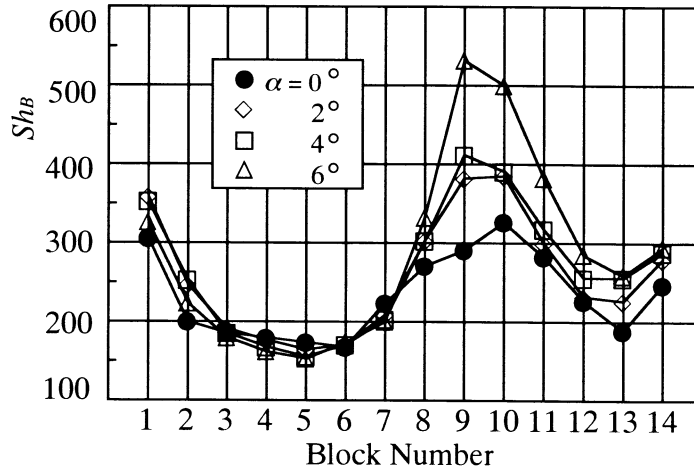
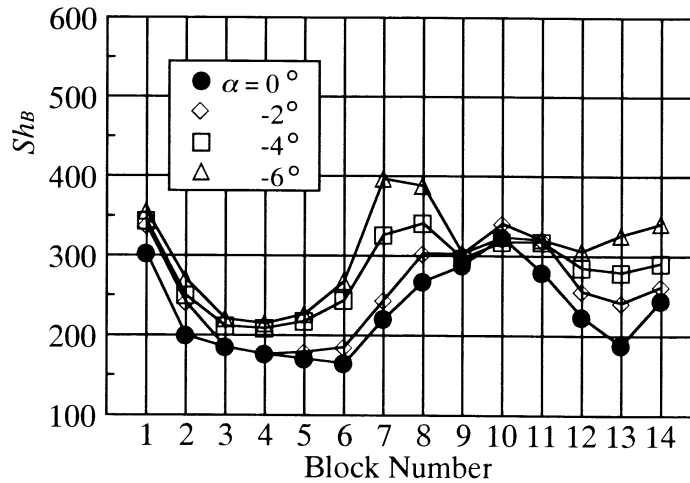


Fig. 4.5 Definition of blocks (divergent channel of  $\alpha > 0^\circ$  and  $C = 50$  mm)

trade-off between the mean heat transfer rate and the pressure loss, the partition wall of the channel should be inclined to the clockwise direction to form the convergent channel of  $\alpha < 0^\circ$ . Details on this subject, including the uniformity in the distributions of the local heat transfer rates, are discussed later in Section 4.4.

#### 4.3.2 Block-Averaged Sherwood Number

In order to grasp the global characteristics of the local mass transfer, we calculated the block-averaged Sherwood number  $Sh_B$  [defined by Eq. (2.4)] for all combination of  $\alpha$  and  $C$ . The blocks are defined in Fig. 4.5; the boundary between Blocks 7 and 8 changes depending on the inclination angle of the partition wall. The streamwise variations of  $Sh_B$  obtained for a medium turn clearance of  $C = 50$  mm are shown in Fig. 4.6. The abscissa shows the block-number defined in Fig. 4.5, and the parameter in the figure is the inclination angle of the partition wall. It was confirmed that  $Sh_B$

(a) Divergent channels ( $\alpha > 0^\circ$ )(b) Convergent channels ( $\alpha < 0^\circ$ )Fig. 4.6 Block-averaged Sherwood numbers ( $C = 50$  mm)

for  $C = 30$  mm and  $70$  mm shows quite similar distributions as Fig. 4.6.

In the divergent channels of  $\alpha > 0^\circ$  shown in Fig. 4.6(a),  $Sh_B$  shows the local maximum at the entrance of the test section and decreases in the flow direction up to Block 6. The influence of inclining the partition wall on the  $Sh_B$  distribution can not be observed so clearly in the region before the turn. In the region after Block 8, namely in the downstream half of the test section, the values of  $Sh_B$  increase as the inclination angle is increased. As a whole, in the present divergent channels, the qualitative characteristics of  $Sh_B$  distributions for smaller  $\alpha$  agree well with those for larger  $\alpha$ . It should be, however, noted that  $Sh_B$  attains the maximum in Block 10 for relatively small  $\alpha$  ( $\alpha = 0^\circ$  and  $+2^\circ$ ) but, in the channels with larger  $\alpha$ , the maximum  $Sh_B$  appears in Block 9 which is located just downstream of the turn section.

Figure 4.6(b) shows the results for the convergent channel. In contrast to the divergent channel in Fig. 4.6(a), the influence of the inclination angle on  $Sh_B$  can be observed in the whole region of the mass transfer test section, and the qualitative characteristics of  $Sh_B$  distribution, as well as quantitative ones, change remarkably with the inclination angle  $\alpha$ . As the inclination of the partition wall is increased,  $Sh_B$  increases in all blocks except for Block 9, and the local maximums of  $Sh_B$  tend to appear not only in Block 10 but also in Blocks 7 and 8, i. e., inside the turn section. The local maximums in Blocks 7 and 8 become larger with the increase in  $\alpha$ , whereas those in Block 10 are almost independent of  $\alpha$ . Under the condition of large inclination angles, quite high values of  $Sh_B$  are maintained in the convergent section after the turn.

From the  $Sh_B$  distributions shown here, it is expected that the uniformity in the distribution of the local heat transfer rates can be improved in the convergent channels, whereas the non-uniformity of the local Sherwood number distribution may be increased in the divergent channels. In order to examine the local heat (mass) transfer characteristics in these channels in more detail, the maps of the local Sherwood numbers are presented in the next section.

#### 4.3.3 Local Sherwood Number Distribution for a Medium Turn Clearance

Figure 4.7 shows the typical distribution of the local Sherwood number  $Sh$  which was obtained in the standard channel with a parallel partition wall ( $\alpha = 0^\circ$ ) and a medium turn clearance ( $C = 50$  mm). Here, at first, the characteristics of  $Sh$  distribution in the standard channel shown in Fig. 4.7 are reviewed briefly. Then,  $Sh$  maps obtained in the channels with an inclined partition wall for the medium turn clearance of  $C = 50$  mm are shown, and in the next section the influence of the turn clearance  $C$  on the local mass transfer characteristics is discussed.

##### (1) Standard channel ( $\alpha = 0^\circ$ )

This result is the same as that shown in Fig. 2.13 but, in order to examine the influence of the inclination of the partition wall on the  $Sh$  distribution, the local heat (mass) transfer characteristics in this standard channel are briefly reviewed here.

In the straight section before the turn of Fig. 4.7,  $Sh$  shows remarkably large values near the entrance of the channel, and then it decreases in the flow direction due to the development of the concentration boundary layer. In the turn section,  $Sh$  increases gradually in the flow direction, and it rises very steeply to attain the local maximums near the junction with the end wall in Block 7 and the junction with the outer wall in Block 8. On the other hand, in the corner of the upstream half of the turn section, there appears a low  $Sh$  region that corresponds to the flow separation caused by the abrupt change of the flow direction.

In the straight section after the turn, there appears a region of relatively low  $Sh$  along the wall

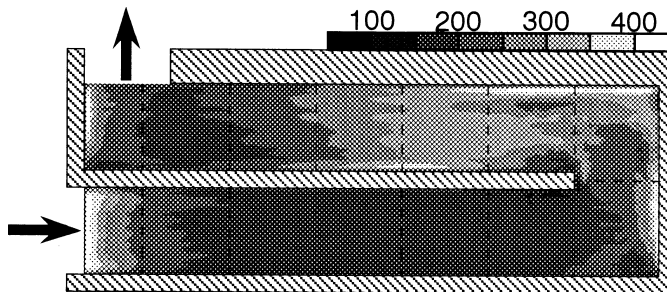


Fig. 4.7 Local Sherwood number distributions in the standard channel ( $\alpha = 0^\circ$ ,  $C = 50$  mm)

near the tip of the partition wall.  $Sh$  then increases in the streamwise direction, and attains the local maximum in Block 10. This means that the flow separates at the partition-wall tip, forms a separation bubble along the partition (inner) wall, and then reattaches in Block 10. In Block 10, the region of high  $Sh$ -values occupies most part of the block and no spanwise deviations are observed in  $Sh$  distribution; thus the location of flow reattachment can not be specified from this  $Sh$  map on the bottom wall. As described in Chapter 2, however, it has been elucidated from the  $Sh$  distributions on all channel walls that this separated flow reattaches on the inner wall.

(2) **Divergent channel ( $\alpha > 0^\circ$ )**

Next, the results obtained in the divergent channels are examined in detail. Figures 4.8 (a), 4.8 (b), and 4.8 (c) show the  $Sh$  maps for  $\alpha = +2^\circ$ ,  $+4^\circ$ , and  $+6^\circ$ , respectively, with a medium turn

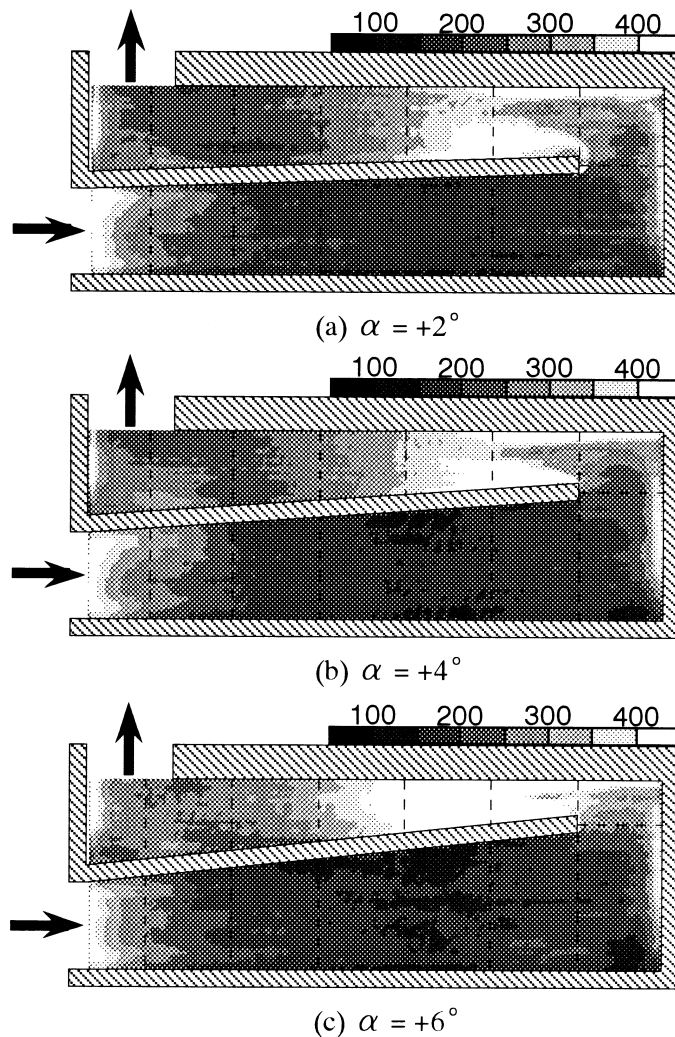


Fig. 4.8 Local Sherwood number distributions in the divergent channels ( $C = 50$  mm)

clearance  $C = 50$  mm. In the divergent section before the turn, there appear the regions of relatively low  $Sh$  near the short-side walls in Blocks 4 and 5, and these low  $Sh$  regions tend to extend toward the central area of the channel as the inclination angle is increased.

In the upstream half of the turn section (Block 7) of all divergent channels presented here, as similar to the standard channel shown in Fig. 4.7,  $Sh$  increases gradually in the flow direction and attains the local maximum near the junction with the end wall. Near the corner in Block 7, the low mass transfer region which corresponds to the flow separation and recirculation can be observed, and  $Sh$  in this region becomes lower as the inclination angle or divergence of the flow passage is increased. As a whole,  $Sh$ -values in the upstream half of the turn section in the divergent channels are smaller than those in the standard channel. In the downstream half of the turn section (Block 8),  $Sh$  shows larger values as  $\alpha$  is increased. Such increase of  $Sh$  in Block 8 with  $\alpha$  can be recognized more clearly from the distribution of block-averaged Sherwood numbers shown in Fig. 4.6 (a), in which  $Sh_B$ -values in Block 8 of the divergent channels are larger than those of the standard channel.

Characteristics of the  $Sh$  distribution after the turn, in Blocks 9 to 14, are much influenced by the inclination angle of the partition wall. At first, the  $Sh$  distribution for  $\alpha = +2^\circ$  shown in Fig. 4.8 (a) is examined in detail. Near the partition-wall tip in Block 9, the region of relatively low  $Sh$  corresponding to a separation bubble is observed, but the scale of this low  $Sh$  region is considerably smaller than that appears in the standard channel shown in Fig. 4.7. Similar to the standard channel,  $Sh$  shows rather high values in a narrow region along the outer wall in and after the turn section (Blocks 8 and 9). The major high  $Sh$  region of Fig. 4.8 (a), however, appears in the partition-wall side after the separation bubble in Blocks 9 and 10 (white region in the figure). Such a deflection of the high  $Sh$  region to the partition-wall side, which was not observed in the standard channel, suggests that the flow separated at the partition-wall tip reattaches on the partition wall. The maximum  $Sh$  that appears in Block 10 is much larger than that observed in the standard channel. After Block 11,  $Sh$  distribution in Fig. 4.8 (a) is quite uniform in the spanwise direction.

As the inclination angle of the partition wall is increased, the values of  $Sh$  in the divergent section after the turn become larger. In Fig. 4.8 (b) showing the  $Sh$  map obtained in the channel of  $\alpha = +4^\circ$ , the low  $Sh$  region corresponding to the separation bubble disappears and  $Sh$  attains the maximum in Block 9, not in Block 10, located just downstream of the turn section. In the channel of  $\alpha = +6^\circ$  shown in Fig. 4.8 (c), the white region of  $Sh > 400$  occupies almost whole area of Blocks 9 and 10 and, as recognized from the  $Sh_B$  distribution shown in Fig. 4.6 (a), the maximum  $Sh$  appears in Block 9 as similar to the channel of  $\alpha = +4^\circ$ . It is thought that such high mass transfer rates near the turn exit for larger inclination angles are caused by the primary flow with high velocity, which is accelerated in flowing through the narrow turn exit, rather than by the reattachment of the flow separated at the partition-wall tip. Because the primary flow after the turn is decelerated in the streamwise direction due to the divergence of the flow passage,  $Sh$  decreases quite rapidly in the flow direction after the high  $Sh$ -values in Blocks 9 and 10. Influence of the inclination angle on  $Sh$ -values can be still observed near the exit of the test section.

### (3) *Convergent channel* ( $\alpha < 0^\circ$ )

The  $Sh$  maps obtained in the convergent channels with  $\alpha = -2^\circ$ ,  $-4^\circ$ , and  $-6^\circ$  are shown in Figs. 4.9 (a), 4.9 (b), and 4.9 (c), respectively. The turn clearance  $C$  is 50 mm in all channels. In the convergent section before the turn, the primary flow is accelerated due to the decrease of the cross-sectional area of the flow passage, and thus  $Sh$  in all convergent channels presented in Fig. 4.9 shows larger values than that observed in Figs. 4.7 and 4.8. As recognized from the  $Sh_B$  distributions as well,  $Sh$  in this section before the turn becomes larger as the inclination of the partition wall is increased.

In the turn section also,  $Sh$  in the channel with a larger inclination angle generally shows higher values. In particular, near the end wall in Block 7 and the outer wall in Block 8, there exist the high

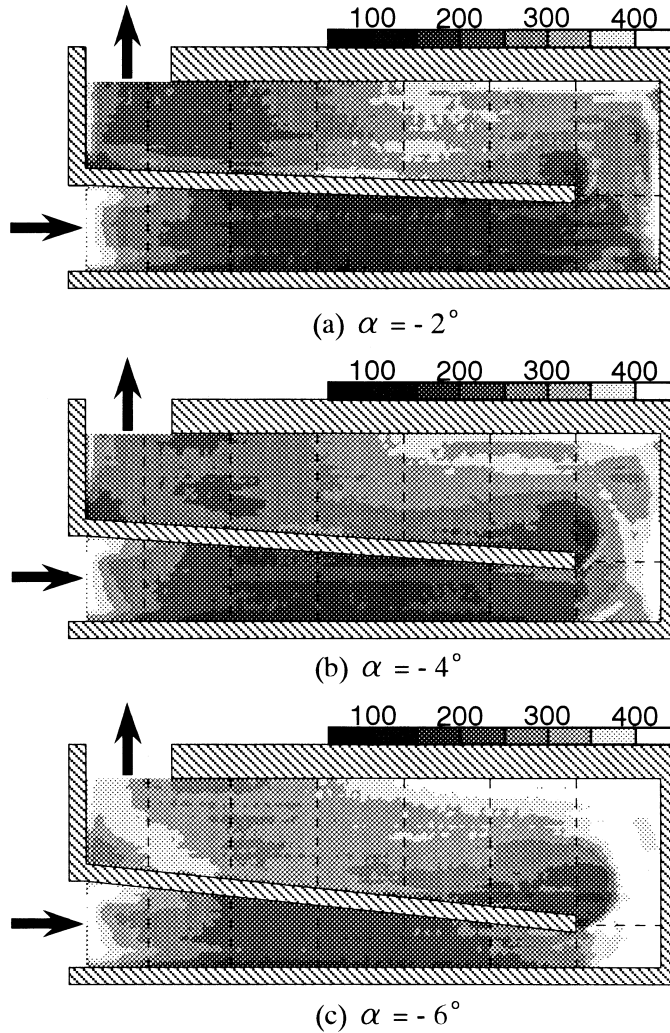


Fig. 4.9 Local Sherwood number distributions in the convergent channels ( $C = 50$  mm)

mass transfer regions of  $Sh > 400$  (white regions). They expand as the inclination of the partition wall is increased and, in the channel of  $\alpha = -6^\circ$  shown in Fig. 4.9 (c), the region of  $Sh > 400$  occupies most part of the turn section. The mechanism of such high mass transfer rates near the short-side walls is considered to be similar to that for the standard channel, and it can be explained as follows. The primary flow that enters the turn section from the convergent section once impinges on the end wall, and then this impinging flow is forced to change its direction by the end wall and it partly impinges again on the long-side wall, i. e., on the mass transfer surface. This second flow-impingement on the long-side wall causes the high  $Sh$ -values near the end wall. As the inclination angle is increased, the cross-sectional area at the turn entrance is decreased and consequently the flow that impinges on the end wall (and on the long-side wall as well) has higher

velocity. As a result, in the convergent channel with a larger inclination angle, the local mass transfer near the end wall is enhanced more effectively. The high  $Sh$  region observed near the outer wall in Block 8 is also produced by the similar mechanism as that near the end wall.

In Block 9 located just downstream of the turn exit, the low mass transfer region which corresponds to the separation bubble is observed near the partition-wall tip of all channels in Fig. 4.9. This low  $Sh$  region occupies larger area than that observed in the standard channel (Fig. 4.7), and it expands upstream toward the turn section (Block 8) as the inclination angle is increased. On the other hand, near the outer wall in Blocks 9 and 10 of the convergent channels,  $Sh$  shows relatively large values. These characteristics of  $Sh$  distribution observed in Fig. 4.9 suggest that, in the convergent channels, a rather large separation bubble is formed near the partition-wall tip, and the separated flow reattaches on the outer wall. The wall on which the flow reattachment occurs in the present convergent channels is just opposite to that in the standard and the divergent channels with  $C = 50$  mm.

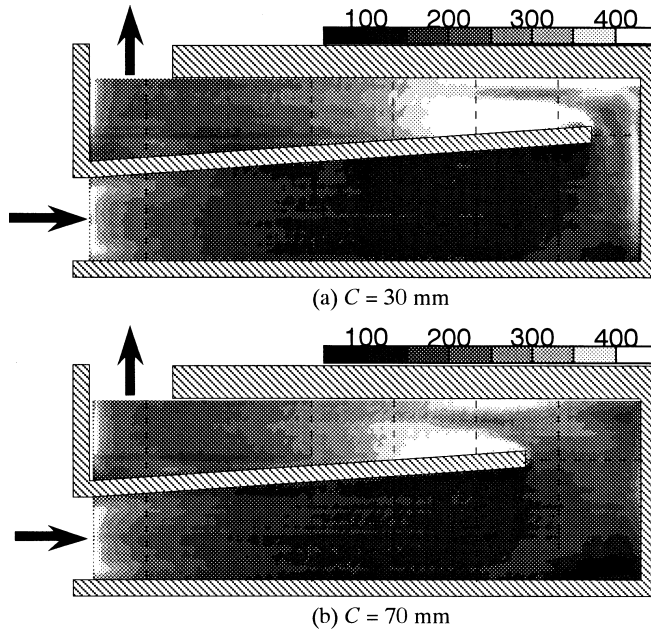
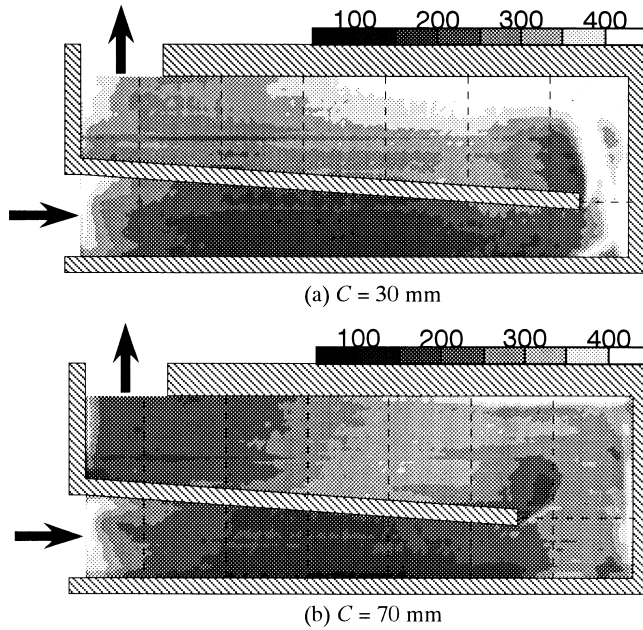
As described above, in Block 9, the low  $Sh$  region near the partition-wall tip and the high  $Sh$  region near the outer wall coexist, and they compensate each other in calculating the block-averaged Sherwood number  $Sh_b$ . This is the reason  $Sh_b$  in Block 9 for the convergent channel, shown in Fig. 4.6 (b), is almost constant irrespective of the inclination angle of the partition wall. After the separation bubble,  $Sh$  in Fig. 4.9 decreases in the streamwise direction; if compared at the same streamwise location,  $Sh$  for a larger inclination angle shows higher values than that for smaller one. It should be also noted that  $Sh$  after Block 11 in the convergent channel is generally larger than that in the corresponding region of the divergent channel.

#### 4.3.4 Influence of Turn Clearance on $Sh$ Distribution

In this section, the influence of the turn clearance on the  $Sh$  distribution is examined in the channels with  $\alpha = +4^\circ$  and  $-4^\circ$ . At first,  $Sh$  distributions in the divergent channels ( $\alpha = +4^\circ$ ) are compared in detail. Figures 4.10 (a) and 4.10 (b) show the  $Sh$  maps obtained in the divergent channels with a turn clearance of  $C = 30$  mm and 70 mm, respectively. In general, global characteristics of the  $Sh$  distributions in the divergent channels with different  $C$  agree qualitatively with one another, albeit some differences are observed in and after the turn section as follows. In the channel with  $C = 30$  mm, the low  $Sh$  region observed in the corner of Block 7 is reduced in scale compared to that in the channel with  $C = 70$  mm, and  $Sh$ -values in the turn section are generally larger than those in other divergent channels with  $\alpha = +4^\circ$ . Near the turn exit,  $Sh$  reaches the local maximum. The value of this local maximum in  $Sh$  for the channel with  $C = 30$  mm is larger than that in the divergent channels with larger turn clearances. Such difference in  $Sh$ -values attributed to the turn clearance, however, diminishes quite promptly, and the values of  $Sh$  near the exit of the test section in Figs. 4.10 (a) and 4.10 (b) are almost in the same level as those observed in the channel with  $C = 50$  mm [Fig. 4.8 (b)]. From a close comparison of  $Sh$ -values in Blocks 11 to 14 in Fig. 4.8 and Fig. 4.10, it follows that in the divergent channels the inclination angle of the partition wall is more dominant to the local mass transfer in this region than the turn clearance.

Next, Fig. 4.11 shows the  $Sh$  maps obtained in the convergent channels ( $\alpha = -4^\circ$ ) with  $C = 30$  mm and 70 mm. In the channel with  $C = 30$  mm shown in Fig. 4.11 (a),  $Sh$  in the downstream half of the test section is much larger than that of the convergent channel with  $C = 50$  mm [Fig. 4.9 (b)] because of the contraction and acceleration of the primary flow through the narrow turn clearance. The qualitative characteristics of the  $Sh$  distribution in the present convergent channel with a narrow turn clearance are, however, quite similar to those with a medium turn clearance. That is, a low  $Sh$  region corresponding to the separation bubble is observed near the partition-wall tip, whereas there appears a high  $Sh$  region along the outer wall.

In the channel with a larger turn clearance of  $C = 70$  mm shown in Fig. 4.11 (b),  $Sh$ -values in and after the turn section are smaller than those in the convergent channel with  $C = 50$  mm. How-

Fig. 4.10 Local Sherwood number distributions in the divergent channels ( $\alpha = +4^\circ$ )Fig. 4.11 Local Sherwood number distributions in the convergent channels ( $\alpha = -4^\circ$ )

ever, the quantitative difference in  $Sh$ -values between the convergent channels with  $C = 50$  mm [Fig. 4.9 (b)] and  $C = 70$  mm [Fig. 4.11 (b)] is not so large as that between  $C = 50$  mm and  $C = 30$  mm [Fig. 4.11 (a)].

In the convergent section after the separation bubble of Fig. 4.11 (b), in Blocks 10 to 14,  $Sh$  shows quite a uniform distribution in the spanwise direction, and the high  $Sh$  region that was observed in the outer-wall side in the channels with narrower turn clearances [Figs. 4.9 (b) and 4.11 (a)] does not appear so clearly. Such a tendency that  $Sh$  distribution after the turn becomes more uniform in the spanwise direction as the turn clearance is increased was also observed in the standard channels described in Chapter 2. Detailed comparison of  $Sh$  in Blocks 11 to 14 in Fig. 4.10 and Fig. 4.11 reveals that the influence of the turn clearance on  $Sh$ -values after the turn appears more clearly in the convergent channels than in the divergent channels. It follows that, in the convergent channels, both the inclination angle of the partition wall and the turn clearance are dominant to the local mass transfer rates after the turn.

#### 4.4 Assessment of Heat-Transfer Performance

As described so far, the heat transfer characteristics and pressure loss in the serpentine channels with a sharp turn are greatly altered by inclining the partition wall. One of the purposes of this study is to find out the optimum combination of the inclination angle and the turn clearance that can achieve both the enhancement of mean heat transfer and the improvement of the local heat transfer uniformity concurrently without a considerable increase of pressure loss. Hence, in this section, the heat (mass) transfer performance of the channels are examined based on the trade-off between the mean mass transfer rates and the pressure loss, and uniformity of the local Sherwood number distributions.

At first, in order to evaluate the increases of mean mass transfer rates and of pressure loss, we have calculated ratio of the mean Sherwood number to the coefficient of flow resistance,  $Sh_m/K$ , and show its variation against  $\alpha$  in Fig. 4.12. In general, the values of  $Sh_m/K$  increase as the turn clearance is increased, and the maximum of  $Sh_m/K$  is found in the channel with  $C = 70$  mm and  $\alpha$

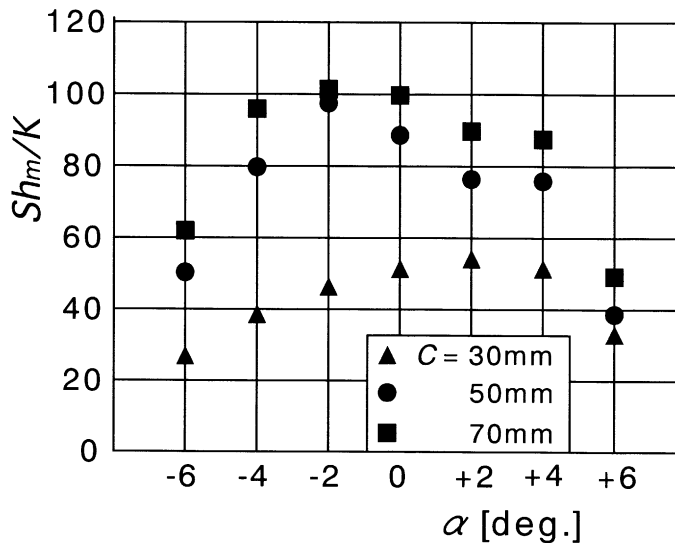


Fig. 4.12 Ratio of mean Sherwood number to coefficient of flow resistance

$= -2^\circ$ . Therefore it follows that, from a viewpoint of the trade-off between the mean mass transfer rates and pressure loss, the highest heat transfer performance can be obtained in the convergent channel with  $C = 70$  mm and  $\alpha = -2^\circ$ . The standard channel ( $\alpha = 0^\circ$ ) with  $C = 70$  mm and the convergent channel with  $C = 50$  mm and  $\alpha = -2^\circ$  also give rather good results.

Next, the uniformity of the local Sherwood number distributions should be examined quantitatively. In order to evaluate it, we have calculated the deviation of the local Sherwood numbers from the mean Sherwood number, i. e.,  $(Sh - Sh_m)/Sh_m$ , and have plotted its frequency in the form of histogram. Figure 4.13 shows the results for  $\alpha = -4^\circ, 0^\circ$ , and  $+4^\circ$  with  $C = 30$  mm, 50 mm and 70 mm. The abscissa shows the values of  $(Sh - Sh_m)/Sh_m$ , and the ordinate shows the frequency, i. e. the number of times. The closer the frequency is distributed around the value of  $(Sh - Sh_m)/Sh_m = 0$ , the more uniform  $Sh$  is distributed over the long-side wall. From this figure, it is found that the frequency tends to concentrate around  $(Sh - Sh_m)/Sh_m = 0$  as the turn clearance is increased, and that the convergent channel ( $\alpha = -4^\circ$ ) gives better uniformity than the standard ( $\alpha = 0^\circ$ ) and divergent ( $\alpha = +4^\circ$ ) channels. Similar trend was also obtained in the channels with other inclination angles.

In order to determine the optimum combination of  $C$  and  $\alpha$  for improving the uniformity of the  $Sh$  distribution, the standard deviation of the local Sherwood number, denoted as  $\sigma$ , has been calculated for all channels tested in this study. The variations of  $\sigma$  against  $\alpha$  are shown in Fig. 4.14. As estimated from the result shown in Fig. 4.13, the values of  $\sigma$  decrease as the turn clearance is increased; the minimum  $\sigma$  can be obtained under the condition of  $C = 70$  mm and  $\alpha = -2^\circ$  or  $-4^\circ$ . Since the lower value of  $\sigma$  corresponds to the higher uniformity of the  $Sh$  distribution, it follows that the combination of  $C = 70$  mm and  $\alpha = -2^\circ$  or  $-4^\circ$ , i. e., convergent channels with a wide turn clearance, is optimum condition for obtaining the most uniform distribution of local heat (mass) transfer rates.

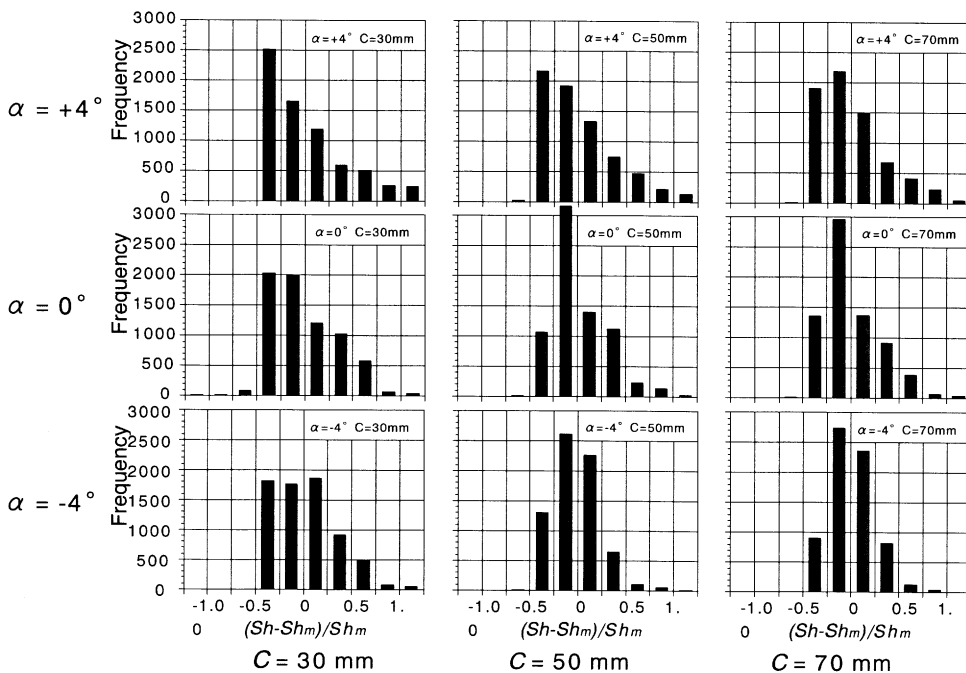


Fig. 4.13 Frequency of deviation of the local Sherwood numbers from the mean Sherwood numbers

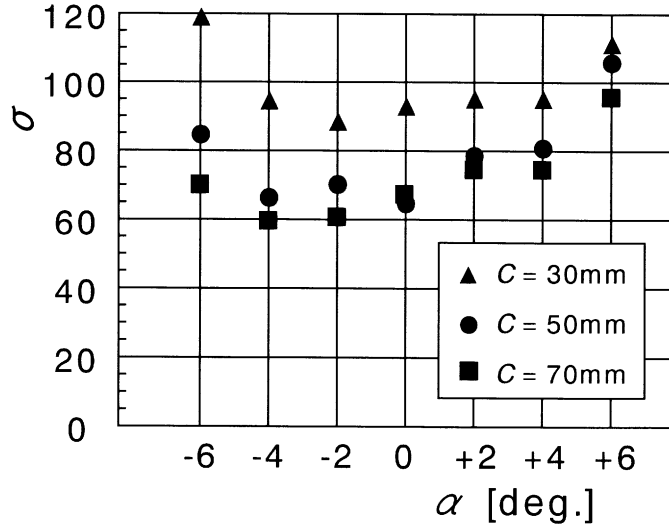


Fig. 4.14 Standard deviation of local Sherwood numbers

From the above-mentioned results of heat (mass) transfer enhancement versus increase of pressure loss, and the uniformity in the distribution of local heat (mass) transfer rates, it can be concluded that the best performance of heat transfer can be achieved in the convergent channel of  $\alpha = -2^\circ$  with  $C = 70$  mm. With this channel, both the enhancement of mean heat transfer and the improvement of local heat transfer uniformity can be achieved concurrently without an increase in the pressure loss. The experimental results described in this paper are limited to the long-side wall of the channel but, at the present stage, it follows that the convergent channel is more advantageous than the divergent channels in the points of both the mean and local heat transfer characteristics.

#### 4.5 Conclusions

In this chapter, the heat (mass) transfer characteristics in the rectangular cross-sectioned serpentine channels with an inclined partition wall have been elucidated; six inclination angles have been tested for three turn clearances under a single Reynolds number. Based on the results of the experiments, the optimum combination of the inclination angle and the turn clearance has been examined from a viewpoint of enhancing the mean heat transfer and increasing the uniformity in the distribution of the local heat transfer rates. Main results are summarized as follows.

(1) In the convergent channels ( $\alpha < 0^\circ$ ), the mean Sherwood number  $Sh_m$  increases as the inclination of the partition wall is increased, whereas  $Sh_m$  in the divergent channels ( $\alpha > 0^\circ$ ) is almost constant or decreased against  $\alpha$ . In general  $Sh_m$  shows higher values as the turn clearance is decreased but, in the divergent channels, the dependence of  $Sh_m$  on  $C$  is rather weak. In both the convergent channels and the divergent channels, the flow resistance increases as the absolute value of  $\alpha$  is increased or as the turn clearance is decreased.

(2) The distribution of the block-averaged Sherwood number  $Sh_b$  in the divergent channels is qualitatively similar to that in the standard channel with a parallel partition wall ( $\alpha = 0^\circ$ ), and the maximum  $Sh_b$  appears after the turn section, in Block 9 (large  $\alpha$ ) or Block 10 (small  $\alpha$ ). On the other hand, in the convergent channels, the qualitative characteristics of  $Sh_b$  distribution, as well as

quantitative ones, change remarkably with  $\alpha$ . As the inclination of the partition wall is increased,  $Sh_B$  increases in all blocks except for Block 9, and the local maximums of  $Sh_B$  appear not only after the turn (in Block 10) but also inside the turn section (in Blocks 7 and 8).

(3) In the divergent channels, the local Sherwood number  $Sh$  before the turn is somewhat smaller than that in the standard channel ( $\alpha = 0^\circ$ ); in the downstream half of the test section, however,  $Sh$  is larger than that in the standard channel and it shows larger values as  $\alpha$  is increased. In the channels of  $\alpha = +4^\circ$  and  $+6^\circ$ , the low  $Sh$  region corresponding to the separation bubble near the partition-wall tip almost disappears, and  $Sh$  attains the maximum in Block 9, not in Block 10, located just downstream of the turn exit.

(4) In the convergent channels,  $Sh$  in the upstream half of the test section is larger than that in the standard channel. After the turn section, quite a large separation bubble is formed near the partition-wall tip, while there appears a high  $Sh$  region near the outer wall.  $Sh$  after the separation bubble increases as the inclination of the partition wall is increased, and it is larger than that in the corresponding region of the divergent channel.

(5) In general, global characteristics of  $Sh$  distributions in the divergent channels with different turn clearances agree qualitatively with one another, and the inclination angle of the partition wall is more dominant to the local mass transfer after the turn than the turn clearance. On the other hand, in the convergent channels, the influence of the turn clearance on  $Sh$ -values after the turn appears more clearly than in the divergent channels. It follows that, in the convergent channels, both the inclination angle of the partition wall and the turn clearance are dominant to the local mass transfer after the turn.

(6) From a viewpoint of enhancing the mean heat transfer and improving the uniformity in the distribution of the local heat transfer rates concurrently without an increase of pressure loss, the best performance of heat transfer can be achieved in the convergent channel with  $C = 70$  mm and  $\alpha = -2^\circ$ .

### Acknowledgements

The authors express their thanks to Mr. N. Shiraki and Mr. K. Tachibana, research engineers in the School of Engineering, for their assistance in producing the experimental apparatus. They also appreciate Mr. S. Araki and Mr. M. Yanagida, graduate students of Department of Mechanical Engineering, for their efforts in conducting the experiments. This study was supported by Electric Power R&D Center, Chubu Electric Power Co., Inc.; the authors express special thanks to Mr. T. Tanaka and Mr. A. Kajita for their cooperation in carrying out this study.

### References

- Astarita, T., Cardone G. and Carlomagno, G. M., *Heat Transfer in Turbulent Flows*, ASME HTD-318, (1995), 161–168.
- Besserman, D. L. and Tanrikut, S., *Journal of Turbomachinery*, **114**, (1992), 865–871.
- Burggraf, F., *Augmentation of Convective Heat and Mass Transfer*, (1970), ASME, New York, 70–79.
- Chyu, M. K., *Journal of Heat Transfer*, **113**, (1991), 63–70.
- Fan, C. S. and Metzger, D. E., *ASME Paper*, (1987), 87–GT–113.
- Goldstein, R. J. and Cho, H. H., *Experimental Thermal and Fluid Science*, **10**, (1995), 416–434.
- Han, J. C., Chandra, P. R. and Lau, S. C., *Journal of Heat Transfer*, **110**, (1988), 91–98.
- Hirota, M., Fujita, H., Yokosawa, H., and Nonogawa, T., *Heat Transfer 3rd UK National Conference Incorporated*

- rating 1st European Conference on Thermal Sciences, **2**, (1992), 923–930.
- Hirota, M., Fujita, H., Tanaka, A., Araki, S. and Tanaka, T., *Energy Conversion and Management*, **38**, (1997), 1155–1168.
- Hirota, M., Fujita, H., Yokosawa, H., Nakayama, T. and Tanaka, T., *Proceedings of the 11th International Heat Transfer Conference*, **5**, (1998), 363–368.
- Hirota, M., Fujita, H., Syuhada, A., Araki, S., Yoshida, T. and Tanaka, T., *International Journal of Heat and Mass Transfer*, **42**, (1999), 3757–3770.
- Hirota, M., Fujita, H., Syuhada, A., Araki, S., Yanagida, M. and Tanaka, T., *Compact Heat Exchangers and Enhancement Technology for the Process Industries*, (1999), 159–166.
- Hirota, M., Fujita, H., Syuhada, Yanagida, M. and Kajita, A., *Proceedings of the 5th ASME/JSME Joint Thermal Engineering Conference*, (1999), AJTE99-6453 (in CD-ROM).
- Johnston, J. P., *Turbulence* (Edited by P. Bradshaw), Chap. 3, (1976), Springer-Verlag, Berlin.
- Kays, W. and Crawford, M. E., *Convective Heat and Mass Transfer*, 2nd ed., p. 197, (1980), McGraw-Hill, New York.
- Liou, T-M., Tzeng, Y-Y. and Chen, C-C., *Journal of Turbomachinery*, **121**, (1999), 569–576.
- Metzger, D. E., Plevich, C. W. and Fan, C. S., *Journal of Engineering for Gas Turbines and Power*, **106**, (1984), 677–681.
- Metzger, D. E. and Sahm, M. K., *Journal of Heat Transfer*, **108**, (1986), 500–506.
- Mochizuki, S., Murata, A., Shibata, R. and Yang, W-J., *Transactions of the Japan Society of Mechanical Engineers*, **64**, (1998), 2216–2223.
- Murata, A., Mochizuki, S. and Fukunaga, M., *Proceedings of the 10th International Heat Transfer Conference*, **4**, (1994), 291–296.
- Sparrow, E. M., and Cur, N., *Journal of Heat Transfer*, **104**, (1982), 82–99.
- Wagner, J. H., Johnson, B. V. and Kopper, F. C., *Journal of Turbomachinery*, **113**, (1991), 321–330.
- Wang, T. S. and Chyu, M. K., *Journal of Thermophysics and Heat Transfer*, **8**, (1994), 595–601.